Schweizerische Eidgenossenschaft
Confédération suisse
Confederazione Svizzera
Confederaziun svizra

Federal Department of
Environment, transport, energy and communication DETEC

**Federal Office of Energy SFOE**
Energy Research and Cleantech Section

**Final report**

---

# HyTES – Optimization of hybrid seasonal heat storage systems using phase change materials

---

**Date:** October 2023, with revisions until June 2024
**Location**: Horw

**Funding provider:**
Federal Office of Energy SFOE
Energy Research and Cleantech Section CH-3003 Bern
www.bfe.admin.ch

**Subsidy recipients:**
Lucerne University of Applied Sciences – Technology and Architecture
Competence Center Thermal Energy Storage
Technikumstrasse 21, CH-6048 Horw
www.hslu.ch/tes

**Author:**
William Delgado-Diaz, Lucerne University of Applied Sciences, williamorlando.delgadodiaz@hslu.ch
Willy Villasmil, Lucerne University of Applied Sciences, willy.villasmil@hslu.ch
Marcel Troxler, Lucerne University of Applied Sciences, marcel.troxler@hslu.ch
Reto Hendry, Lucerne University of Applied Sciences, reto.hendry@hslu.ch
Philipp Roos, Lucerne University of Applied Sciences, philipp.roos@hslu.ch
Jörg Worlitschek, Lucerne University of Applied Sciences, joerg.worlitschek@hslu.ch

**BFE department head:** Andreas Eckmanns, andreas.eckmanns@bfe.admin.ch
**BFE program management:** Stephan Mathez, stephan.a.mathez@solarcampus.ch
**BFE contract number:** SI/502171-01

# Summary

Switzerland's Energy Strategy 2050 mandates an increase in renewable energy-sourced heat production and the expansion of seasonal heat storage to reduce grid dependency. This study addresses the limitations of traditional solar thermal and seasonal storage systems, such as living space occupation, additional summer heating, and high costs, by optimizing a seasonal hybrid heat storage system. The proposed solution integrates a buried hybrid thermal energy storage system using water and encapsulated Phase Change Materials (PCM), coupled with a Photovoltaic (PV) system and a heat pump (HP).

Our findings demonstrate that thermal self-sufficiency (SSth) of up to 85% is achievable with an ~8m³ storage system for a multifamily house with 20 inhabitants, while maintaining reasonable costs. Beyond this capacity, costs and volumes increase exponentially. For SSth below 70%, the system costs are comparable to the existing systems but offer a significantly better Global Warming Potential (GWP) than the oil boiler base case. Maximizing PV capacity and selecting an appropriate HP are confirmed as essential prerequisites for ensuring the effectiveness of Thermal Energy Storage (TES) in enhancing thermal self-sufficiency. Overall, the study highlights the necessity of policies to drive renewable heating solutions with respect to still low-cost fossil fuel solutions.

This study introduces, for the first time, a deeply comprehensive model of hybrid sensible-latent thermal energy storage, featuring a fixed bed of randomly arranged PCM macrocapsules. The model considers effects at different scales, from stratification in the sensible part to melting-crystallization effects of various capsule geometries and considers operations from system to component level. Additionally, a complete optimization was performed, considering techno economic and GWP analyses, to derive Pareto front solutions encompassing main component sizes and the internal topology of the hybrid TES.

Our research underscores the feasibility and benefits of hybrid systems in meeting renewable energy targets, demonstrating substantial economic and environmental advantages through a model that is both deep in its detail and wide in its scope.

# Résumé

La Stratégie Énergétique 2050 de la Suisse impose une augmentation de la production de chaleur à partir d'énergies renouvelables et l'expansion du stockage thermique saisonnier pour réduire la dépendance au réseau. Cette étude aborde les limitations des systèmes thermiques solaires traditionnels et de stockage saisonnier, telles que l'occupation de l'espace de vie, le chauffage supplémentaire en été et les coûts élevés, en optimisant un système de stockage thermique hybride saisonnier. La solution proposée intègre un système de stockage d'énergie thermique hybride enterré utilisant de l'eau et des matériaux à changement de phase (MCP) encapsulés, couplé à un système photovoltaïque (PV) et à une pompe à chaleur (PAC).

Nos résultats démontrent qu'une autonomie thermique (SSth) allant jusqu'à 85 % est réalisable avec un système de stockage d'environ 8 m³ pour une maison multifamiliale avec 20 habitants, tout en maintenant des coûts raisonnables. Au-delà de cette capacité, les coûts et les volumes augmentent de manière exponentielle. Pour une autonomie thermique inférieure à 70 %, les coûts du système sont comparables à ceux des systèmes existants, mais offrent un potentiel de réchauffement global (PRG) nettement meilleur que la chaudière à fioul de référence. Maximiser la capacité PV et sélectionner une pompe à chaleur appropriée sont confirmés comme des conditions préalables essentielles pour assurer l'efficacité du stockage d'énergie thermique (TES) en améliorant l'autonomie thermique. Globalement, l'étude souligne la nécessité de politiques pour encourager les solutions de chauffage renouvelable face aux solutions à combustibles fossiles encore peu coûteuses.

Cette étude introduit, pour la première fois, un modèle profondément complet de stockage thermique hybride sensible-latent, comprenant un lit fixe de macrocapsules MCP disposées aléatoirement. Le modèle prend en compte les effets à différentes échelles, de la stratification dans la partie sensible aux effets de fusion-cristallisation de diverses géométries de capsules, et considère les opérations du niveau système au niveau composant. De plus, une optimisation complète a été réalisée, en prenant en compte des analyses technico-économiques et de PRG, afin de dériver des solutions de front de Pareto englobant les principales tailles de composants et la topologie interne du TES hybride.

Notre recherche souligne la faisabilité et les avantages des systèmes hybrides pour atteindre les objectifs d'énergie renouvelable, démontrant des avantages économiques et environnementaux substantiels grâce à un modèle à la fois détaillé et de grande envergure.

# Zusammenfassung

Die Energiestrategie 2050 der Schweiz verlangt eine Erhöhung der Wärmeproduktion aus erneuerbaren Energien und den Ausbau der saisonalen Wärmespeicherung, um die Abhängigkeit vom Stromnetz zu verringern. Diese Studie befasst sich mit den Einschränkungen traditioneller solarthermischer und saisonaler Speichersysteme – wie der Beanspruchung des Wohnraums, zusätzlicher Sommerheizung und hohen Kosten – durch die Optimierung eines saisonalen hybriden Wärmespeichersystems. Die vorgeschlagene Lösung integriert ein vergrabenes hybrides thermisches Energiespeichersystem, das Wasser und verkapselte Phasenwechselmaterialien (PCM) verwendet, gekoppelt mit einem Photovoltaik-(PV)-System und einer Wärmepumpe (WP).

Unsere Ergebnisse zeigen, dass eine thermische Selbstversorgung (SSth) von bis zu 85 % mit einem Speichersystem von etwa 8 m³ für ein Mehrfamilienhaus mit 20 Bewohnern erreicht werden kann, während die Kosten angemessen bleiben. Jenseits dieser Kapazität steigen die Kosten und Volumina exponentiell an. Bei einer SSth von unter 70 % sind die Systemkosten vergleichbar mit bestehenden Systemen, bieten jedoch ein deutlich besseres Globales Erwärmungspotenzial (GWP) als der Öl-Heizkessel als Vergleichsbasis. Die Maximierung der PV-Kapazität und die Wahl einer geeigneten WP sind als wesentliche Voraussetzungen für die Wirksamkeit der thermischen Energiespeicherung (TES) zur Verbesserung der thermischen Selbstversorgung bestätigt worden. Insgesamt hebt die Studie die Notwendigkeit von politischen Maßnahmen hervor, um erneuerbare Heizlösungen angesichts weiterhin kostengünstiger fossiler Brennstoffe voranzutreiben.

Diese Studie stellt erstmals ein umfassendes Modell für hybride sensible-latente thermische Energiespeicherung vor, das ein Fest Bett aus zufällig angeordneten PCM-Makrokapseln umfasst. Das Modell berücksichtigt Effekte auf verschiedenen Skalen, von der Schichtung im sensiblen Teil bis zu Schmelz-Kristallisationseffekten verschiedener Kapsel Geometrien, und betrachtet die Betriebsweise sowohl auf System- als auch auf Komponentenebene. Zudem wurde eine vollständige Optimierung durchgeführt, bei der techno-ökonomische und GWP-Analysen berücksichtigt wurden, um Pareto-Front-Lösungen zu ermitteln, die die Hauptkomponentengrößen und die interne Topologie des hybriden TES umfassen.

Unsere Forschung unterstreicht die Machbarkeit und die Vorteile hybrider Systeme zur Erreichung der Ziele für erneuerbare Energien und zeigt erhebliche wirtschaftliche und ökologische Vorteile durch ein Modell, das sowohl in seiner Detailtiefe als auch in seinem Umfang überzeugt.

# Table of contents

# 1 Introduction

## 1.1 Background and State of the Art

Implementing the Energy Strategy 2050 calls for a major increase in heat production from renewable energy sources and a significant expansion of the capacity for seasonal heat storage. Currently, the household sector in Switzerland holds the most energetic and economic potential for heat storage. This is because households account for about 50% of heat consumption and use more than 80% of their final energy for space heating and hot water [1]. To boost the share of renewable energies and self-sufficiency, seasonal heat storage is essential, making it a crucial technology for realizing the Energy Strategy 2050 [2]. Although the current focus to achieve the objectives comprises mainly district heating-oriented solutions, equally viable alternatives are necessary for buildings outside the effective range of these large systems.

Despite their importance, only a few seasonal heat storage systems have been implemented in Switzerland so far. Examples include the multi-family solar houses in Oberburg and Huttwil, built by Jenni Energietechnik AG [3]. The sensible heat storage devices, located centrally in the buildings as thermally insulated steel tanks, are charged using thermal solar collectors. The main drawbacks of this approach are: (I) loss of living space, (II) unwanted additional heating of the building in summer due to storage heat losses, and (III) a lack of flexibility due to total dependence on solar energy. The OPTSAIS project revealed that the Levelized Cost of Energy Storage (LCOES) for such sensible seasonal heat storage is quite high [4]. One of the main reasons for this is the costly living space taken up by the tank. To ensure 100% self-sufficiency (even in worst-case scenarios of low solar radiation and low external temperatures), the storage and solar system must be oversized, increasing system costs. Alternatively, backup solutions, like wood chip heating, must be used in winter, bringing in additional investment and/or operational costs.

The system examined in this project involves seasonal hybrid heat storage (using water along with phase change materials), which is operated together with photovoltaics (PV) and a heat pump. This system has a key advantage over conventional systems with solar thermal systems: it offers flexibility and a consistent energy supply all year round. If the storage unit lacks energy (due to higher heat demands or low solar yield), this can be compensated for with grid electricity using the existing heat pump. Therefore, the storage and PV system do not need to be oversized for worst-case scenarios, and integrating alternative backup solutions is not necessary as the system can guarantee the services even with an empty storage tank.

In addition, placing the storage unit underground completely removes the largest cost factor, which is the occupation of living space. However, reducing storage volume is still crucial with this setup, as the excavation costs of buried storage rise significantly with increased volume, especially with increasing tank height [4]. Additionally, reducing storage volume means that the container surface, and therefore heat losses, are minimized, which is a vital aspect when optimizing seasonal heat storage.

In tandem with these strategies, our project also considers the overall Global Warming Potential (GWP) of the system and how to minimize it while maintaining performance. This objective aligns cohesively with our pursuit of minimizing storage volume and optimizing the overall size of various components. The emphasis on component size reduction is not solely a cost-containment measure but also a deliberate strategy to minimize the environmental footprint of the system. By concurrently addressing financial and environmental concerns, we seek to foster a model that is both economically viable and ecologically responsible. This dual-focused approach underscores our commitment to implementing the Energy Strategy 2050 in a manner that not only satisfies energy demands but also is conscientious of our global environmental impact.

## 1.2 Motivation

While the Energy Strategy 2050 primarily emphasizes thermal grids for seasonal storage, exploring alternative options for residences beyond the optimal thermal districts' viable range is crucial. Given the swift electrification of the energy system, it is imperative to identify alternative solutions that not only ensure services with minimal environmental impact but also provide grid flexibility by incorporating renewable energy without isolating from the overall energy system.

A method to achieve reduced storage volume involves enhancing the storage's energy density. Integrating encapsulated Phase Change Materials (PCM) into sensible heat storage emerges as a proficient solution. During PCM phase transitions, a notable amount of latent thermal energy is consistently absorbed or released, contingent upon the material. Introducing PCM capsules into sensible storage allows for a volume reduction between factors of two to five, while maintaining equivalent storage capacity and depending upon the system configuration. The utility of PCM becomes particularly significant when the temperature differential between the storage's loaded and unloaded states is minimized, owing to the increased latent to sensible heat ratio, favoring latent storage.

Hybrid storage advantages extend beyond merely increasing energy density; they also encompass improved thermal stratification and temperature stabilization in areas where PCM is employed [5]–[7]. The enhancement of thermal stratification, resulting from combining sensible and latent heat storage, has been affirmed in various applications [8]. As revealed in the BFE project OPTSAIS, exclusive stabilization of the storage's upper area temperature can curtail storage volume by up to 40%[4], [9].

The thermal conductivity of PCM, notably in its solid state, is comparatively low, resulting in reduced thermal output. Since seasonal storage systems do not necessitate substantial thermal outputs, with loading and discharging durations extending from weeks to months, the requirement for heat transfer between storage water and PCM is not pressing. This enables the utilization of larger capsules, likely between 1 to 10 liters, positively influencing the encapsulation costs and the PCM to encapsulation cost ratio. Abundant and affordable available salt hydrate based PCMs (below 1 CHF/kg) imply that appropriate PCM selection can potentially facilitate economic and competitive seasonal storage systems.

This project aims to identify the system's optimal configurations, with a focus on seasonal hybrid storage that yields the lowest system costs and global warming potential, while achieving a degree of self-sufficiency between 70 and 100% for space heating and domestic hot water provision. To determine the optimal configuration, key considerations include the PV installation size, heat pump, thermal energy storage units, as well as the material, placement, and size of the PCM capsules.

## 1.3 Research questions.

The main objective of this project is to analyze and minimize costs and global warming potential by reducing the volume of a seasonal hybrid heat storage system and other components in the system, utilizing a combination of water and encapsulated Phase Change Materials (PCM) as the storage medium. The system under consideration involves a buried hybrid heat storage, a Photovoltaic (PV) system, and a heat pump (HP), aiming for high solar coverage or a degree of thermal self-sufficiency between 70 and 100% of the total heat requirement (space heat and domestic hot water) for a representative Swiss Multi-Family House (MFH) in a specified reference scenario.

To achieve this objective, the following research questions were addressed:

- How effectively can integrating PCM capsules reduce the storage volume and thereby the costs of a seasonal heat storage device?
- What is the optimal configuration for the heat storage concerning PCM, including size, shape, quantity, and placement?
- What are the ideal configurations for the entire system regarding the ratios between PV area, Heat Pump (HP) output, and storage volume?
- What are the costs associated with each component of the system?
- How do the costs correlate with the desired level of self-sufficiency?

# 2 Methodology

## 2.1 System description

The overall system is presented in Figure 1. Essentially, it consists of the system model (and component models), the NOMAD optimizer and pre- and post-processing modules.

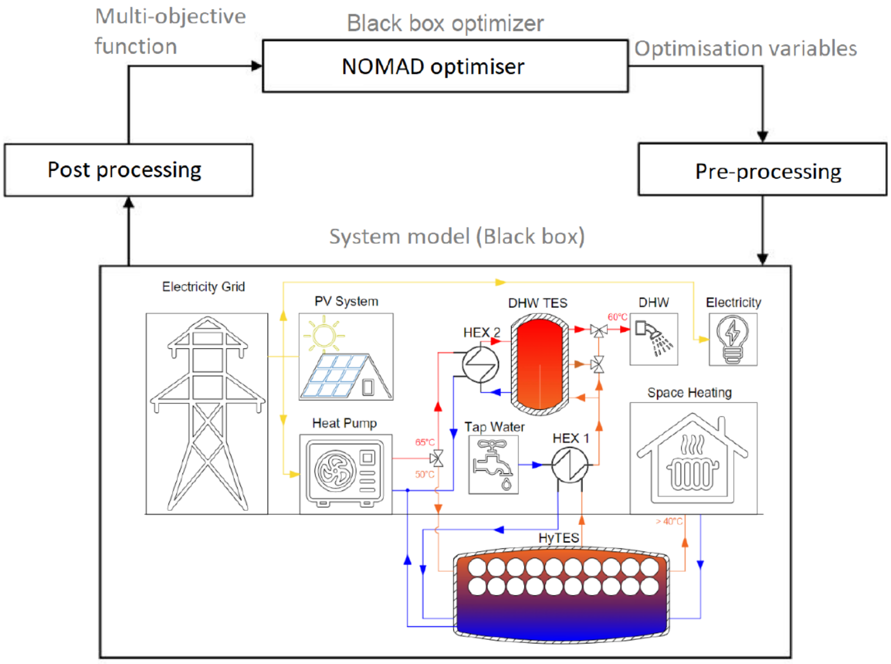

Figure 1 Diagram of the entire system, abbreviations: photovoltaics (PV), heat pump (WP), heating system (HS), domestic hot water.

The system model represents the model examined and is implemented in C++. The investigated configuration consists of: (I) a buried thermal storage filled with PCM capsule, (II) a PV system, (III) a heat pump and (IV) a representative apartment building. The storage, the PV system and the heat pump are implemented as physical models in the system. The building is mapped based on typical consumption profiles (heating requirements, domestic hot water, and electricity requirements). The PV system produces electricity during the day, depending on the weather. This electricity is first used to cover the residents' own electricity needs. The heat pump operates with the surplus. If the PV system does not supply enough or excess electricity, the required electricity can be obtained via the grid connection or excess electricity can be fed into the grid.

The energy required for the DHW and HS should, if possible, always be provided directly with the heat pump and PV electricity to minimize exergy losses. If this is not possible, the required energy is taken from the storage. If the storage unit cannot supply the energy either, the energy is provided using the heat pump and grid electricity. The storage system stores the excess thermal energy from the heat pump with PV electricity and releases it when required. Heat losses through the storage wall are considered.

The main optimization parameters focus on the sizes of the different components such as installed PV, HP power, storage geometry and volume, PCM capsule size, number of capsules and capsule position in the storage. The algorithm performing the black box optimization, NOMAD optimizer [10] as well as the objective function, based on a combination of KPIs that reflect the objectives of the optimization are further described in Section 2.5.

The preprocessing routine generates the required input data for the system model for each run. Post-processing uses the stored data from the simulation and the optimization parameter sizes from NOMAD to determine the optimization objective using costs, global warming potential and thermal self-sufficiency.

For each storage concept, described in Section 2.2, optimization runs were carried as follows: The optimizer defines a set of parameters based on the optimization domain defined, and passes them on to preprocessing.

The preprocessing module generates the required input data for the system and component models with each iteration based on the feedback from NOMAD. The system simulation is then executed with the given inputs. The termination criterion is the achievement of a "steady state" or a previously defined maximum annual repetition. In this context, "steady state" means that the difference in the energy content of the storage at the end of the year compared to the energy content at the beginning of the same year must not exceed 5%. If this is exceeded, another year is simulated, with the temperature distribution in the storage at the beginning of the year corresponding to that at the end of the previous year.

Once the simulation of the system model is finished, the post-processing calculates all different energy flows, capital and operational expenditure of the simulated systems based on the comprehensive cost function library generated and discussed in Section 2.5.1. This allows the determination of the optimization objective function at the end of each iteration, key input for NOMAD to set up the next run. The value is then returned to the optimizer, whereupon new inputs are prepared, and another set of runs is started. The optimization is stopped when either an optimum has been found or a defined number of runs has been completed.

## 2.2 Boundary conditions and scenarios

This section describes the different boundary conditions, fixed parameters and scenarios considered within the project, which include building information including location and weather conditions, as well as service energy demands in addition to the information of the considered PCMs and PV panels.

### Reference apartment building

The size of the apartment building and the number of residents have a direct influence on the space heating and hot water requirements of the building. A detailed analysis of the Swiss building stock was carried out in the BFE project OPTSAIS [4] to define a representative reference for an apartment building. To allow comparisons with the storage system defined in the OPTSAIS project, the same reference building was adopted. Due to the use of PV modules, it was assumed that the MFH was equipped with a flat roof. The most important building features are listed below:

- Number of apartments: 8 (two per floor)
- Living space per apartment: 100 $m^2$ (4 rooms)
- Energy reference area: 800 $m^2$
- Total available roof area: 264 $m^2$
- Number of residents: 20 people

### Location and weather

The location of the reference building determines the weather conditions (solar radiation and outside temperature) required for the dynamic simulations. There is no geographical location in Switzerland that can be considered "representative" of Swiss weather. For this reason, the city of Bern, as in the

OPTSAIS [4] project , was chosen as the location as it has the highest density of buildings with 6 - 9 apartments.

The weather parameters required for the models are air temperature, global and diffuse horizontal radiation. The data used for the simulation was obtained from Meteonorm [11], from the Zollikofen weather station (BE). Zollikofen is the closest weather station to the city of Bern where calculated data on solar radiation is available. Climate values are used as data, with the period of temperature parameters considering the years 2000-2019 and the period of radiation parameters considering the years 1996-2015. The data is averaged hourly.

### Space heating requirement

The reference apartment building has a space heating requirement of 30 kWh/m2/a and should be heated to a target temperature of 20°C during the heating period. It is assumed that underfloor heating is an emitter system in the building. The flow temperature of the heating is approx. 35°C and the return temperature is 25°C. The corresponding hourly heating power profile was created using the “Heating Degree Day” and “Heating Degree Hour” methods, with 12°C being assumed as the limit temperature. Taking the capacity and inertia of the house into account, the hourly values were filtered using a moving average with a 6-hour window.

### Domestic hot water requirement

A central issue in the treatment of domestic hot water (DHW) is the prevention of legionella in the drinking water system. In order to avoid Legionella, the concepts and the minimum DHW temperatures are considered as in SIA 385/1:2020 [12]. Depending on the type of treatment, the minimum DHW temperature in the storage tank can vary in the range of 55-58°C.

On average, each person in Switzerland uses around 50 liters of hot water at 60°C per day [13] [14]. Since 20 people live in the reference apartment building, 1 $m^3$ of hot water must be provided every day. It is assumed that the tap water has a temperature of 10°C. The final profile fed to the model is generated using DHWCalc v2.02b [15] which generates DHW draw profiles based on statistical methods and the total daily requirements.

### Electricity requirement

The electricity requirement was implemented as a standardized, variable annual load profile using measurement data from HTW Berlin, which measures purely electrical load profiles with 1 hour resolution, publishes them and offers them for download [16]. Two specific electricity load profiles were extracted from this data set and averaged and then passed on to the simulation as a normalized time profile based on the total yearly consumption. The normalization step allows the load profile to be scaled to the respective estimated annual consumption of the building based on data form SFOE for single and multi-family dwellings based on the amount of inhabitants. [17]

### Storage scenarios

Figure. 1shows the three different storage concepts with the different cases examined in this study. All storage units except for concept 3 are buried in the ground outside the building to avoid any influence on the living space.

In concept 1, cylindrical double-walled Vacuum Insulated Tanks (VIT) are examined. Due to the low thermal conductivity of the vacuum, such storage units offer stable long-term thermal insulation performance. Conventional insulation materials cannot offer such solutions because the absorption of soil moisture leads to a significant increase in thermal conductivity. However, the production of such a storage unit is associated with high costs and global warming potential. Since the costs for excavation increase disproportionately from a depth of 4 m, the storage height is limited to 4 m.

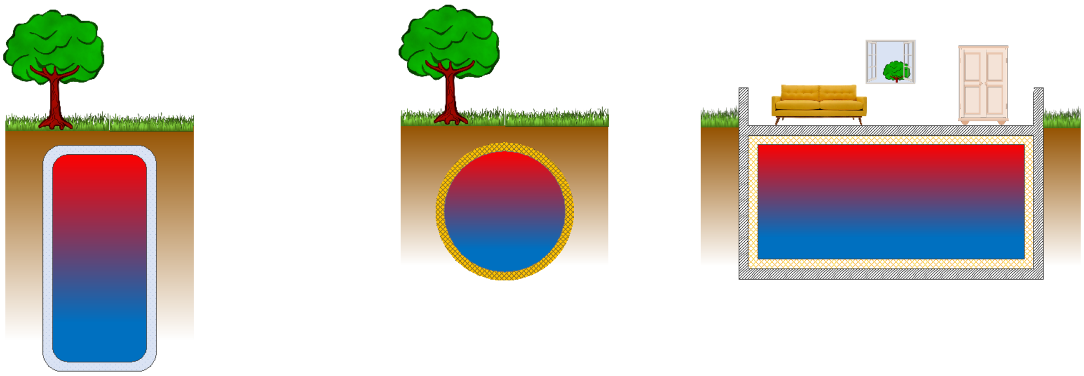

Figure. 1: The three storage concepts considered in the project with the different cases

In concept 2, thermal storage is examined based on the structure of the company energ4me. These are Spherical Storage Tanks (SST) made of glass fiber reinforced plastic. A 0.3 m PUR foam layer is applied as thermal insulation. The capacity of such a storage facility is limited to a maximum of 14 m $^{3}$, due to practical and transportation constraints. The company energ4me has already sold several storage devices and they are operating successfully.

In concept 3, the focus is on the use of existing, unused basement space already available, and is thus referred to as Repurposed Basement Storage (RBS). The idea is to convert existing rooms into a thermal storage facility by applying suitable waterproof thermal insulation materials. This concept is being developed within the GEAS project [18], a collaboration between HSLU and Swisspor, funded by Innosuisse. The reuse of the space is expected to result in significant cost reductions, as virtually the only costs associated are the advanced insulations materials and installation. The height of the storage is limited to the average basement ceiling height, between 2 and 3 meters.

### PCM properties

The PCMs that are introduced into the seasonal heat storage have a major influence on the energy density of the system, its efficiency, and costs. To use the most accurate data possible, PCMs developed by COWA TS are considered, for which measured and tested thermophysical properties and cost data supported by supplier offers are available. The considered PCM properties are shown in Table 1 and they all correspond to materials currently under development at COWA TS, with PCM-4 having already reached market applications. Additionally, as they are all SAT based, the global warming potential calculations consider them equally and do not require further adjustment. As the mass fraction of different additives for the different PCMs is within the same order of magnitude for the four cases, COWA TS projects the costs of all variations around the same price and similar thermophysical properties.

| | **PCM-1** | **PCM-2** | **PCM-3** | **PCM-4** | |
|---|---|---|---|---|---|
| **Nominal melting temperature** | 40 | 42 | 45 | 48 | °C |
| **Phase change enthalpy** | 241 | 178 | 208 | 210 | kJ/kg |
| **Specific heat capacity liquid** | 3.1 | 3.1 | 3.1 | 3.1 | kJ/ (kg K) |
| **Specific heat capacity fixed** | 2.9 | 2.9 | 2.9 | 2.9 | kJ/ (kg K) |
| **Density liquid** | 1.3 | 1.3 | 1.3 | 1.3 | kg/l |
| **Density fixed** | 1.3 | 1.3 | 1.3 | 1.3 | kg/l |
| **Price** | 1.0 | 1.0 | 1.0 | 1.0 | CHF/kg |

Table 1 PCM used, based on the latest findings from Cowa TS, all based on SAT + Additives.

### Additional assumptions

It is assumed that the storage units are operated at atmospheric pressure. The room temperature in the building is controlled at 20°C and the incoming tap water is at a constant 10°C.

As the primary energy supply, the PV system has several potential optimization variables. However they were fixed for the Suntech Ultra S mini [19] a largely used model in Switzerland, with an established market and supply chain. In Table 2 the main properties of the panel are shown.

| Properties | Value |
|---|---|
| **Maximum Power [kWp]** | 0.380 |
| **Efficiency [%]** | 20.8 |
| **Solar cell [-]** | Monocrystalline silicon |
| **Height [mm]** | 1756 |
| **Width [mm]** | 1039 |
| **Thickness [mm]** | 35 |
| **Weight [kg]** | 20.3 |

Table 2 Overview of properties of Suntech Ultra S mini.

## 2.3 Numerical modeling

The implemented system model encompasses three physical and three boundary condition component models. The physical component models include: (1) thermal energy storage model, (2) PV module model, and (3) heat pump model. The boundary condition models cater to: (1) domestic hot water demand, (2) space heating demand, and (3) electricity demand.

To intricately describe the complex dynamics of individual physical components and their interactive behavior, a system of differential equations is utilized. The PV module and the heat pump are modeled using ordinary differential equations, with variables dependent on time, while the thermal hybrid energy storage is described through coupled energy conservation equations. These component models are interconnected, facilitating data transmission amongst them in a complete system model.

Incorporating insights from the BFE project “OPTSAIS” [4], the in-house thermal energy storage model for sensible heat storage, SolTES, was adopted and further enhanced with a latent model[20]. Furthermore, portions of the PV model were derived from the EU project Heat4Cool [21], [22].

The model operates with two time loops: an inner and an outer loop. In the inner time loop, the energy conservation equations of the thermal storage are solved, utilizing a time step that is smaller than the outer time step. Conversely, the outer time step not only determines the recalculations for the PV module and the heat pump but also establishes the intervals for data transfer and acquisition from the boundary condition models. Consequently, this data establishes the boundary conditions for each physical model for the succeeding outer time step.

### 2.3.1 Storage model (SolTES)

The thermal hybrid energy storage model consists of three energy equations. Equation 1 describes the temperature distribution in the liquid medium, Equation 2 describes the temperature distribution in the capsule material and Equation 3 describes the temperature distribution of the PCM in a spherical shape.

Coupling terms link the energy equations together and source and sink thermals add or remove thermal energy into or from the storage. The following assumptions were made:

- In Equation 1 and 2 radial temperature gradients are neglected
- In Equation 1 and 2 there is no phase change
- All flows are fully developed.
- Convection effects within the storage and in the PCM are neglected.
- Properties of water (capacity, density, conductivity) are independent of temperature.

$$\begin{aligned}\phi_{lqd}\rho_{lqd}c_{p,lqd}\frac{\partial T_{lqd}}{\partial t} + \phi_{lqd}u\rho_{lqd}c_{p,lqd}\frac{\partial T_{lqd}}{\partial z} \\ = \lambda_{lqd}\frac{\partial^2 T_{lqd}}{\partial z^2} + q_{lqd,cap} + \sum q_{source} - \sum q_{sink}\end{aligned} \tag{1}$$

$$\phi_{cap}\rho_{cap}c_{p,cap}\frac{\partial T_{cap}}{\partial t} = \lambda_{cap}\frac{\partial^2 T_{cap}}{\partial z^2} + q_{cap,lqd} + q_{cap,pcm} \tag{2}$$

$$\rho_{pcm}\frac{\partial h_{pcm}}{\partial t} = \frac{1}{r^2}\frac{\partial}{\partial r}\left(\lambda_{pcm}r^2\frac{\partial T_{pcm}}{\partial r}\right) + q_{pcm,cap} \tag{3}$$

This includes $\phi$ the volume fraction, $\rho$ the density, $c_p$ the specific heat capacity, $T$ the temperature, $u$ the speed of the liquid medium, $z$ the direction (starting from the bottom of the storage), $\lambda$ the heat transfer coefficient, $h$ the specific enthalpy and $r$ the radius of the PCM capsule, considered as spherical.

The coupling terms $q_{lqd,cap}$ and $q_{cap,lqd}$ couple the energy Eq. 1 and Eq. 2 and $q_{cap,pcm}$ and $q_{pcm,cap}$ couple the energy Eq. 2 and Eq. 3 and are described as follows:

$$q_{lqd,cap} = U\frac{A_{cap}}{V}f_{cap}\left(T_{cap} - T_{lqd}\right) \tag{4}$$

$$q_{cap,lqd} = U\frac{A_{cap}}{V}f_{cap}\left(T_{lqd} - T_{cap}\right) \tag{5}$$

$$q_{cap,pcm} = U\frac{A_{cap}}{V}f_{cap}\left(T_{pcm} - T_{cap}\right) \tag{6}$$

$$q_{pcm,cap} = U\frac{A_{cap}}{V}\left(T_{cap} - T_{pcm}\right) \tag{7}$$

Where $U$ represents the total heat transfer coefficient, $A$ the heat transfer area of a capsule, $V$ the volume and $f_{cap}$ the number of capsules in a storage layer.

The source and sink terms can be described as follows:

$$\sum q_{source} + \sum q_{sink} = U_{loss}A_{loss}\left(T_{lqd} - T_{sur}\right) + \sum_k \frac{\dot{m}_k c_{p,lqd}}{V}\left(T_{lqd} - T_{k,noz}\right) \tag{8}$$

The first term describes the losses of the storage compared to the environment and the second term describes the introduction of thermal energy into the storage and the removal from the storage via various nozzles.

A nodal mixing model determines the effects of buoyancy-induced mixing. Increases in fluid density at lower temperatures cause cooler layers to sink and warmer layers to rise. The nodal mixing model assumes a point in time at which a warmer layer $i$ + 1, located beneath a cooler layer $i$, completely mixes, and reaches a uniform temperature. This is expressed by:

$$T_{i+1}^{neu} = T_i^{neu} = \frac{m_i c_{p,i} T_i + m_{i+1} c_{p,i+1} T_{i+1}}{m_i c_{p,i} + m_{i+1} c_{p,i+1}} \tag{9}$$

The finite volume method is used to discretize the equations. A uniform cell size is used for equation 9. Non-uniform cell sizes can be used for the energy Eq. 1 and Eq. 2. This increases the positioning flexibility of the capsule layer in the storage and increases the simulation accuracy and speed, since the cell sizes at the corresponding positions for both energy equations are the same, but larger cells can be selected in non-overlapping, sensible areas. The central differentiation scheme is used for the spatial discretization of the diffusion terms. The convection term in equation 1 is discretized using the updraft/downdraft scheme. Implicit backward differentiation scheme is used for temporal discretization.

The thermophysical properties of the water and the capsule material are independent of temperature. The water values used correspond to a temperature of 35 °C.

However, the thermophysical properties of the PCM are different for the two different aggregate states, liquid and solid, regardless of temperature. During the phase change process, the specific heat capacity must be determined based on a defined melting range as follows:

$$c_{p,pcm,fus} = \frac{\Delta h}{T_{pcm,f} - T_{pcm,s}} \tag{10}$$

The enthalpy of fusion $T_{pcm,f}$is $\Delta h$ the temperature at which the PCM is completely liquid and $T_{pcm,s}$the temperature at which it is completely solidified. Additionally an approximate skewed normal distribution approach as described by Ashour et Al [23] was used to provide a continuous heat capacity function that includes the phase change enthalpy within the melting range defined by the manufacturer. Figure 2 shows an example of the used heat capacity function implemented in the model.

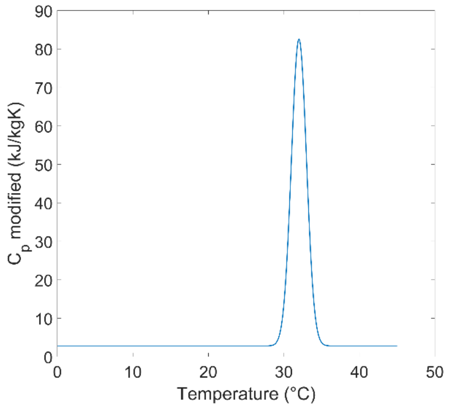

Figure 2 Continuous specific heat capacity function, including the phase change enthalpy for simulations.

The implemented energy Eq. 3 assumes a spherical capsule geometry. Thus, for any alternative capsule shape, the geometries are approximated using a hollow sphere of equal surface and volume as a spherical capsule equivalents [22]. The equivalent spherical capsule is generated with identical surface, thickness of the capsule material and PCM quantity to the alternative shape. Due to the minimal surface area to volume ratio of a sphere, a cavity is assumed in the center of the sphere as shown in Figure 3 to compensate for the volume difference.

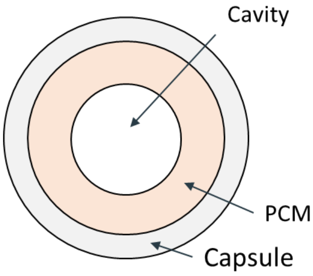

Figure 3 Hollow sphere approximation for PCM capsule calculations.

### 2.3.2 Losses, ground temperature and assumptions on the losses.

To appropriately account for the energy losses over the year, it is necessary to account for the interaction of the TES with the surrounding soil.

To do so, the method proposed by Marquez et al.[24] was implemented to calculate the undisturbed temperature distribution in the soil based on the weather data, and average soil properties. As shown on Eq. 11. The undisturbed ground temperature profiles can be calculated throughout the year using an analog simple harmonic function.

$$T_{soil}\left(z,t\right) = T_m - T_p \mathrm{e}^{-z\sqrt{\frac{\omega}{2\alpha}}} \cos\left(\omega t - \varphi - z\sqrt{\frac{\omega}{2\alpha}}\right) \qquad (11)$$

Where $T_m$ corresponds to the annual average temperature on the location of interest, $T_p$ is the annual amplitude of the monthly average temperature cycle, $\omega$ the annual temperature cycle in radians per second, *f* is the phase (normally 0 to avoid time shifts) and $\alpha$ is the ground thermal diffusivity given by the ratio of ground thermal conductivity and the product of density and heat capacity of the soil.

Figure 4 shows a sample of the expected undisturbed soil temperatures at the chosen HyTES reference building up to 5 m in depth through the year.

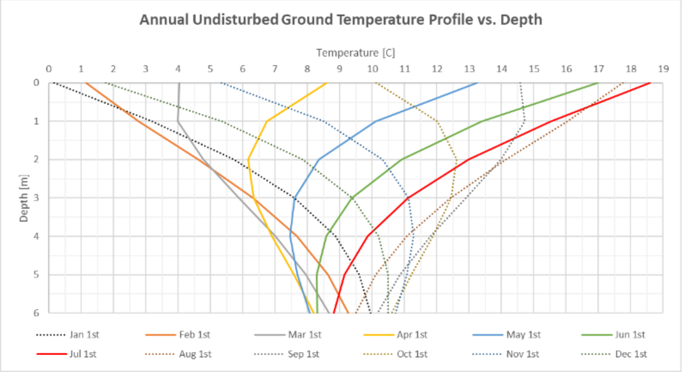

Figure 4. Undisturbed ground temperature distribution at reference building location.

Figure 5 Temperatures on the top and bottom of the soil layer around the TES tank. shows the temperatures on the top and bottom surfaces of the ground layer ($d_{ground}$) around cylindrical tank throughout the year. For practical purposes, the actual profile applied on the vertical side surface is not shown as it oscillates between the two limits shown.

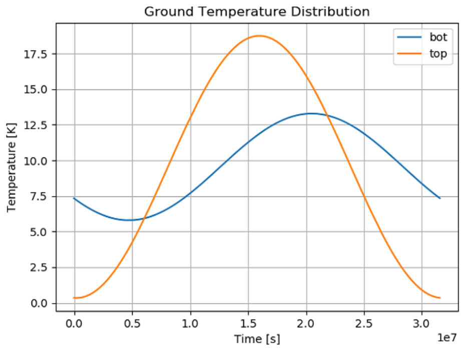

Figure 5 Temperatures on the top and bottom of the soil layer around the TES tank.

The influence of the temperature fluctuations and the ground capacity surrounding the storage was studied using a version of the system model that considers the ground capacity around the storage as additional instances of the SolTES component model. This required a computational time increase for the test cases of around 80%, as effectively 3 instances of the SolTES need to be executed for a single underground storage (and two adjacent layers of ground), in addition to the required additional iterations overall to reach steady state of the added capacities.

These effects exponentially add up computational time on a robust optimization procedure, and thus it was considered unfeasible in the framework of the optimization. However, these simulations allowed the estimation of the area of influence of the storage on the ground surrounding it and how it also requires time to reach steady state.

Figure 6 shows an example of the results produced with this method for the temperatures in the bottom of the tank, and adjacent ground layers.

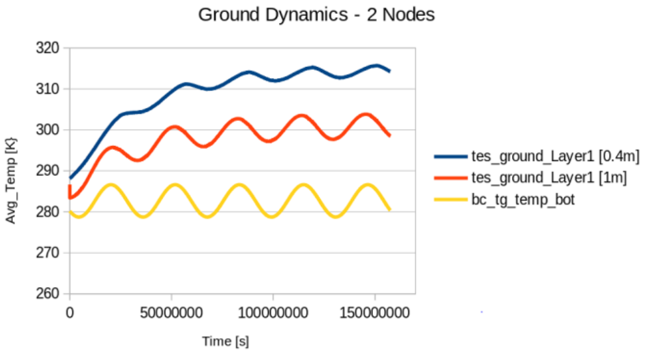

Figure 6 Ground dynamics for two additional instances of SolTES acting as ground surrounding the storage. ($d_{Ground}$ = 0.4m and 1m)

Using the results of the ground capacity simulations a layer of ground of fixed thickness ($d_{Ground}$ = 1m) was implemented to account for the thermal resistance of the TES surroundings along with undisturbed ground temperature profiles are used as the boundary conditions on the outer surface of the soil layer as shown in Figure 7. As the performance of the system is considered once it reaches a yearly steady state, the model assumes an additional resistance zone that is a close representation of the behavior of a realistic underground TES in a steady state.

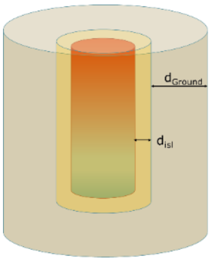

Figure 7. Representation of affected ground volume around TES and thermal insulation.

### 2.3.2 PV module model

The electricity generated by the PV system is calculated using the model by A. Bellini et al. [25] seen below in Eq. 12:

$$I_P = I_{SC}(G_{GTI}, T)\left[1 - C_1\left(e^{\left(\frac{V_P}{C_2 V_{OC}}\right)} - 1\right)\right] \tag{12}$$

Where $I_P$ corresponds to the module current, $I_{SC}$ the “short circuit” current, $V_P$ the module voltage, $V_{OC}$ the “open circuit” voltage and $C_1$ and $C_2$ coefficients. All parameters required for determining the two coefficients as well as for $I_{SC}$ and $V_{OC}$ are specified by the manufacturers on the module data sheet.

The global oblique irradiation $G_{GTI}$ on the PV module is determined as follows:

$$G_{GTI} = G_{BTI} + G_{DTI} + G_{RTI} \tag{13}$$

The direct oblique radiation $G_{BTI}$ and reflected oblique radiation $G_{RTI}$ were taken from [26]. The diffuse oblique radiation $G_{DTI}$ was determined using the Perez model [26]. The NOAA algorithm [27] was used to calculate the sun azimuth angle and the sun position angle.

### 2.3.3 Heat pump model

The thermal energy of the heat pump is determined using the following Eq. 14 through 16 [28]:

$$\dot{Q}_{hp} = \dot{m}_{sink}\, c_{p,sink}\left(T_{sink,out} - T_{sink,in}\right) \tag{14}$$

$$P_{ele} = \frac{\dot{Q}_{hp}}{COP_{real}} \tag{15}$$

$$COP_{real} = \phi\ COP_{carnot} = \phi\ \frac{T_{sink,out}}{T_{sink,out} - T_{sour,in}} \tag{16}$$

Where $\dot{Q}_{hp}$ is the thermal performance of the heat pump, $P_{ele}$ the electrical power consumed, $COP_{real}$ the real COP value of the heat pump , $\phi$ the quality level of the heat pump and $COP_{carnot}$ the Carnot COP value of the heat pump.

The quality level of the heat pump is also recalculated on every time step based on the temperature differences across the heat pump. To do so, the following function is used based on the regression for operating points of Siemens EUTEQ heat pump.

### 2.3.4 System integration description

The system combines a Seasonal Hybrid TES (SHTES), a domestic hot water tank (HWTES), a set of photovoltaic panels (PV), and a heat pump (HP) to provide space heating (BC SH) and domestic hot water (BC DHW) services to a multi-family house (see Figure 8). The building’s consumption is mapped using typical consumption profiles (heating through heating degree days model, and domestic hot water and electricity requirements).

Figure 8 shows a detailed diagram of the interconnection of the different component models.

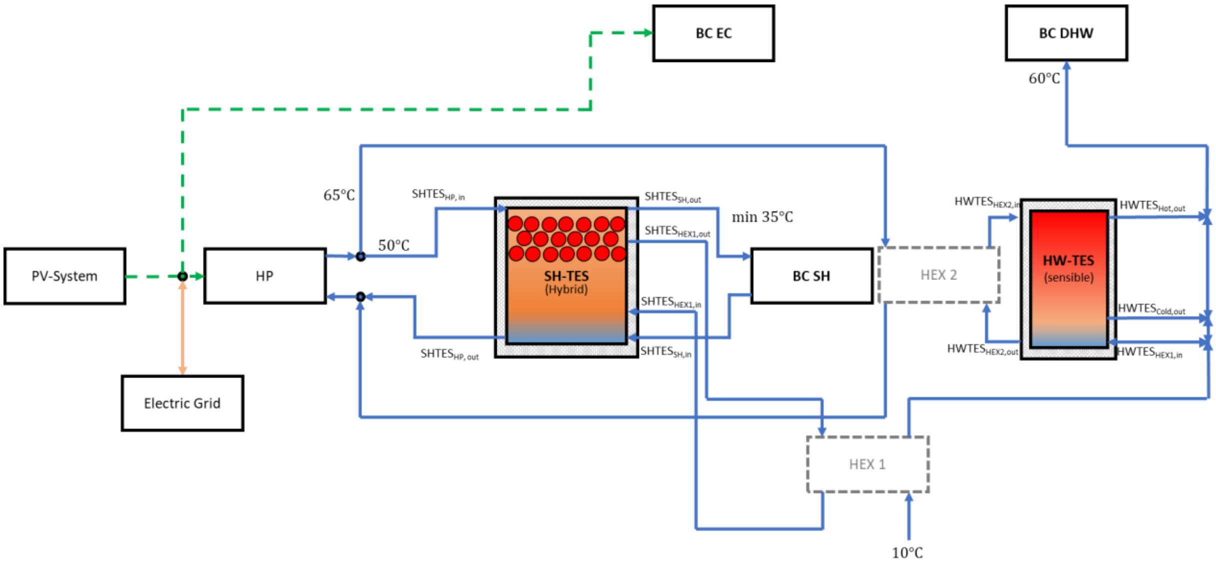

Figure 8 Diagram of the system model and different connections.

The building's PV system serves as the entire system's primary energy source, powering the residents' electricity needs and the heat pump for both thermal services. The electricity grid supplements the PV system if there is insufficient power at any given point to maintain the comfort level around 100%.

A valve controls the sink side of the heat pump, which directs a heat flow of 65°C to the HWTES or a 50°C heat flow into the underground SHTES. The SHTES and the HWTES are separate tanks due to the requirements for DHW to prevent legionella in drinking water systems. The minimum DHW temperature in the storage tank can vary from 55-58°C [14], and by separating the tanks, the SHTES can stay at a lower temperature than the DHW temperature standard. This approach minimizes the losses in the SHTES tank over extended periods and gives more flexibility for the independent operation of both services. By keeping the HWTES a sensible heat storage, it can deliver the high power required for DHW service, compared to a system with PCM capsules.

The HWTES can be placed somewhere in the building, while the SHTES tank is buried underground. To minimize energy and exergy losses, the air/water HP and PV directly supply the necessary energy for DHW and SH whenever possible storing the excess in the TES tanks.

The heat flow goes through the SHTES and directly to the space heating system. The SH needs a minimum temperature of 35°C, to guarantee a large enough temperature difference with the room temperature and thus the minimum temperature is also considered before supplementary energy from the grid is drawn. The maximum temperature of the SHTES tank is 50°C, enough for the PCM to melt and maintain a temperature difference, but as low as possible to reduce losses to the ground. By monitoring the outlet temperature of the storage and considering both ports for HP and SH system are at the same height in the hybrid storage, we gain the advantage of a bypass with the bonus of directly using the heat pump and storing any excess energy in a single step.

The rule-based controller used can be summarized in the following main steps:

1. Fulfill electrical demand with PV whenever possible.

2. If surplus PV power is available provide space heating directly with HP and PV (through LHTES bypass) and store the remaining energy in SHTES.
3. Use SHTES if no PV power is available to provide space heating service.
4. If SHTES$_{SH,out}$ drops below 35C use grid electricity and HP to provide the service and partially charge the storage if there is excess heat produced by HP.
5. If PV power is available, no space heating is required and SHTES is nearly full (95%), use the HP and PV to charge the HWTES.
6. If by nighttime the HWTES is still partially charged, use grid electricity and HP to charge the specified buffer zone of HWTES (1m3).

The HWTES is heated to a maximum of 65°C by the heat pump via HEX 2. The DHW system begins by using cold tap water that is pre-heated with the SHTES tank through a heat exchanger (HEX 1). The coupling of SHTES and HWTES relieves the heat pump from heating cold tap water to a high-temperature level. It also allows for the DHW service to be partially provided by the SHTES tank, which in turn is charged with solar power, as opposed to the HP having to charge the HWTES on grid electricity fully.

After pre-heating, the tap water flows to the HWTES. To maintain the maximum temperature of 60°C of the DHW service (in case the HWTES is fully charged to 65°C) the hot and cold outlets as well as the incoming pre-heated tap water are mixed to match the required outlet temperature. Table 3 summarizes how the DHW service fulfilment strategy works.

| Case | Conditions | Operation mode |
|---|---|---|
| **1** | $HWTES_{Cold,out} \geq 60\ ^{\circ}\mathrm{C}$ | Water from HWTES$_{Cold,out}$ and preheated fresh water are mixed to 60 °C. |
| **2** | $HWTES_{Cold,out} < 60\ ^{\circ}\mathrm{C}$<br>$HWTES_{Hot,out} \geq 60\ ^{\circ}\mathrm{C}$ | Water from HWTES$_{Hot,out}$ and HWTES$_{Cold,out}$ are mixed to 60 °C. |
| **3** | $HWTES_{Cold,out} < HWTES_{Hot,out} < 60\ ^{\circ}\mathrm{C}$ | DHW cannot be supplied at the required temperature of 60 °C. Uses HWTES$_{Hot,out}$ only. |

Table 3 Domestic hot water demand fulfillment strategy.

## 2.4 Global warming potential estimation

This section describes the methodology for the integration of a global warming potential (GWP) estimation functionality. It evaluates the GWP throughout the life cycle of main components, including the PV system, heat pump, various Hybrid Thermal Energy Storage units, and the DHW TES.

It excludes aspects like heat distribution systems, heat exchangers, valves, and piping since their contribution is assumed to be negligible compared to the main components. The system's GWP is split into production and disposal, and operational phases. The production and disposal GWP are fixed, determined by component size, and unaffected by system operation, and the operational GWP is influenced by the required grid electricity use only.

This chapter first examines and parametrizes each component's fixed GWP of production and disposal. It then accounts for the operational phase's GWP concerning grid electricity use before finally integrating all data as functions into the model.

### 2.4.1 PV panels

The Global Warming Potential (GWP) of Photovoltaic (PV) panels across their entire lifecycle remains fixed, unaffected by their electricity production levels [29]. A report by R. Frischknecht et al., under the 'International Energy Agency', conducted a thorough Life Cycle Assessment (LCA) on 3 kWp residential PV systems in Europe in 2020, exploring various PV technologies and life cycle stages, including manufacturing, transport, and end of life management [30]. The study highlights a 30-year lifetime for panels and a 15-year lifetime for inverters, with a linear degradation of electricity output at 0.7% per annum. Notably, the bulk of a PV system's emissions are tied to its manufacturing phase. Additional studies, including one by the Swiss Federal Office for the Environment in 2018, affirm these findings, revealing a consistent GWP for silicon-based panels and an average GWP for solar energy of 0.0417 kg CO2-eq kWh−1 in Switzerland [29], [31]–[33]. Calculating GWP per kWp involves multiplying the discovered g CO2-eq kWh−1 for each technology by the presumed total electricity produced over the 30-year lifespan.

$$\text{Total Electr.} = \sum_{i=1}^{30} PR \times (1 - ADR)^{i} \tag{17}$$

Where PR represents the initial energy production rate in kWh per kWp at peak performance (975 kWh $kWp^{-1}$), and ADR represents the annual degradation rate as a percentage (0.7%). The expression $(1 - ADR)^{i}$ represents the fraction of energy produced relative to the previous year, considering the annual degradation rate. When multiplying this with the CO2−eq kWh−1 for each technology, the following total GWP per kWp over their lifetime is:

- CdTe: 696.4 kg CO2−eq kWp−1
- CIS/CIGS: 954.0 kg CO2−eq kWp−1
- Multi-Si: 1111.7 kg CO2−eq kWp−1
- Mono-Si: 1116.9 kg CO2−eq kWp−1

To calculate the amount of GWP attributed to the PV system, the above values can be multiplied by the total installed max power of the system.

### 2.4.2 Heat pump.

Research indicates that the Global Warming Potential (GWP) of various heat pump types is predominantly influenced by the electricity utilized during their operational lifetime, rather than their construction [34]–[37]. The GWP varies significantly across regions due to the diverse regional electricity GWPs. The construction and end-of-life (EOL) phases of heat pumps contribute merely 2-4% to the total GWP, although their significance amplifies with lower electricity GWP. Data from Switzerland’s Federal Office for the Environment (SFOE) was utilized to evaluate the GWP of heat pumps, providing inventories for 7, 15, and 50 kW air-water heat pumps [38].

Heat pump components, primarily composed of steel and copper, have material amounts determined by scaling from average weights of multiple pumps, with energy production data sourced from Viessmann Werke GmbH [39]. Assumptions for standard transport distances adhered to the Ecoinvent methodology [40]. Recyclable materials, including steel, copper, and coolant R410a, are distinguished from non-recyclable materials, which are incinerated. Refrigerant emissions comprise 3% filling loss during manufacturing and 19% upon disposal, totaling 22%. Additional emissions include electrical input converted into waste heat. Heat pumps are disposed of in compliance with EU standards, classifying them as industrial devices subject to Waste from Electrical and Electronic Equipment (WEEE) regulations and hazardous waste incineration. Initially, 85% of the refrigerant input is disposed of, assuming a 15% loss, while remaining metal fragments are recycled.

The LCA results from the report for each heat pump power capacity are shown in Table 4.

| No. | **HP [kW]** | **GWP [kgCO$_{2\text{-eq}}$]** |
|---|---|---|
| **1** | 7 | 3,060 |
| **2** | 15 | 3,670 |
| **3** | 50 | 13,700 |

Table 4 Overview of the total GWP of the three investigated heat pump power capacities (HPC) excluding the use phase [53].

These values can predict the GWP of other capacities, assuming the same trend applies. Eq. 18 and Figure 9 present the quadratic equation used to estimate GWP of the heat pump.

$$GWP_{HP}(HPC) = 4.8912 \cdot HPC^2 - 31.356 \cdot HPC + 3039.8 \qquad (18)$$

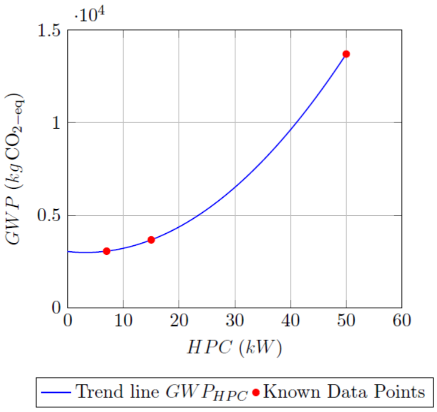

Figure 9 Plot of GWP for various HPCs according to Equation 20 over the known data points [38].

### 2.4.3 Thermal Energy Storage

The evaluation of the Global Warming Potential (GWP) of heat storage spans various scenarios, among them, dedicated Domestic Hot Water (DHW) storage tanks and three different scales of large underground storage. L. Sztranyovszky’s internal HSLU Life Cycle Assessment (LCA) study, titled "Comparative Life-Cycle Assessment of Energy Storage Technologies for Photovoltaic-Heat Pump Systems of Single-Family Houses," forms the basis for determining the GWP of DHW storage, VIT storage, and Phase Change Material (PCM) capsules.

Adopting a cradle-to-grave system boundary, the study intentionally omits the use phase and applies two distinct system models: cut-off and consequential. The primary Life Cycle Impact Assessment (LCIA) methodology employed is Ecoinvent EF3.0, enriched by supplementary methods ReCiPe 2016 (H) and Cumulative Energy Demand for comprehensive comparison.

### DHW Storage Tank

The tank under consideration has a 2.5mm thick wall made of stainless steel (18/8) and holds a volume of 600l. It is also insulated with a 120mm layer of glass wool. When it reaches its end-of-life (EOL), the Life Cycle Assessment (LCA) predicts that the steel is recycled as mixed metal scrap, while the glass wool is sent to a landfill, and any remaining materials are incinerated.

The LCA points out that a 600l insulated tank has a Global Warming Potential (GWP) of 770 kg CO2-eq (GWPT600l). It is assumed that both the surface area and the GWP scale linearly with the materials used. To derive an equation for the GWP of a Domestic Hot Water (DHW) tank as a function of its volume (GWPDHW(V)), Equation 19 is utilized. In this equation, the known GWP of the 600l tank is divided by its calculated surface area, thus producing effectively a specific GWP per surface of the DHW tank.

$$GWP_{DHW}(V) = \frac{GWP_{600l}}{A_{DHW}(600)} \cdot A_{DHW}(V) \qquad (19)$$

### Encapsulated PCM

The HyTES project utilizes High-Density Polyethylene (HDPE) capsules filled with a Sodium Acetate Trihydrate (SAT)-based PCMs. Each capsule, with an outer volume of 0.135l, encompasses SAT, Glycine, Borax (anhydrous), and HDPE. The LCA addresses the manufacturing process, which encompasses injection and blow molding using virgin HDPE granulation, PCM mixing and filling, and additional processes. Post-use, the analysis presumes distinct management of plastic and PCM waste, with the latter being dispatched to landfills as inert waste.

The investigation reveals a GWP of 488 kg CO2-eq per 1000 capsules (each 0.135 l), with an assumption that GWP scales linearly with capsule volume as 90% of the GWP is attributed to the volume of materials as shown in Figure 10. Consequently, minor variations in capsule volume will result in minimal deviations allowing for the calculation of the GWP for a single capsule as shown in Equation 20.

$$GWP_{Cap}(V_{cap}) = \frac{\left(\frac{GWP_{1000-capsules}}{1000}\right)}{0.135 \cdot 10^{-3}} \cdot V_{cap} \qquad (20)$$

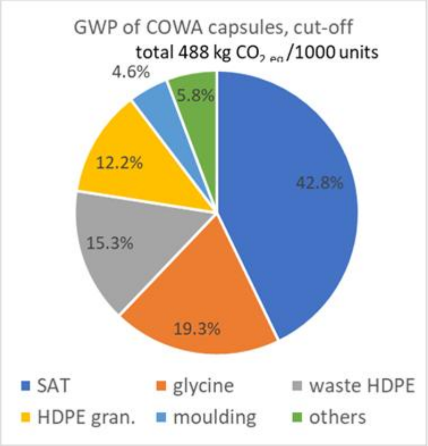

Figure 10 Main contribution for GWP of COWA capsules according to L. Sztranyovszky, Appendix B.

To take the capsules into account for the different storages in the modelling of the system, the amount of capsules depends on the storage volume (V) and packing density (PD). Equation 21 describes the GWP of the capsules per volume of storage (GWP1000−capsules). Here the GWP$_{Cap}$ (V$_{Cap}$) is multiplied by the number of capsules, which is the total volume multiplied by the PD, both divided by the V$_{Cap}$.

$$GWP_{Capsules}(V, V_{Cap}, PD) = GWP_{Cap}(V_{cap}) \cdot \frac{V \cdot PD}{V_{cap}} \tag{21}$$

**Vacuum Insulated Tank (VIT)**

The first considered underground storage is the vacuum insulated tank (VIT). Data provided by Sirch Vacutherm is used [41] to estimate the GWP of the production of such tanks. The two main components are considered, the PCM capsules and the vessel containing them. The estimation is made as a function of the storage volume.

Data from the LCA of L. Sztranyovszky is used again to consider the production of the tank. Besides the GWP of the 600l storage tank, the study also specifies the weight of the steel tank. When the GWP$_{600l}$ is divided by the weight (90kg), a constant of GWP per kg of the storage tank is generated (GWPVIT−weight, in kg CO2 kg−1 of tank). To use this for the VIT, the GWP per kg of VIT is assumed to be double that of the 600l tank, considering a double layer of steel.

$$GWP_{VIT-weight} = 2 \cdot \frac{GWP_{600l}}{W_{600l}} = 2 \cdot \frac{770}{90} = 17.12 \tag{22}$$

Next, the weight of the VIT must be parameterized. The parametrization is done with data from the ’tank configurator’ of Sirch standard tanks, which specifies the weights for many tank volumes [42]. The function of the storage volume is based on this data, using the weights and corresponding volumes to generate a second-order polynomial trend line. This data is plotted in a spread plot, like in Figure 15, on which quadratic regression was applied to create Weight$_{VIT}$ (V).

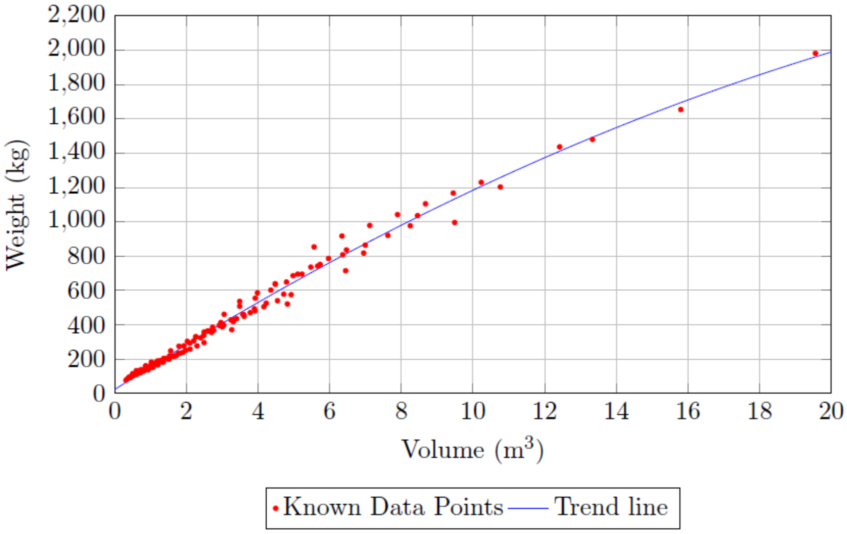

Figure 11 Trendline based on known data points from Sirch [59].

Finally, both Equation 22 and $Weight_{VIT}$ (V) can be combined with the GWP of the capsules to calculate an estimate of the GWP of VIT; see Equation 23. This equation is not an exact way to consider the GWP of the VIT system, as it only roughly considers the vessel production.

$$GWP_{VIT}(V) = GWP_{VIT-weight} \cdot Weight_{VIT}(V) + GWP_{Capsules}(V) \tag{23}$$

### Spherical Storage Tank (SST)

The Spherical Storage Tank (SST) that is considered for the HyTES project is the enerSAFE storage tank, see Figure 12 from Energy4Me. The tank consists of two layers of Glass-Fiber Reinforced Plastic with a thickness of 7mm each, with a vacuum in between, and a 25cm layer of Polyurethane Foam (PUR)

Figure 12 Spherical-shaped storage enerSAFE from Energy4Me [43].

The Global Warming Potential (GWP) of a storage unit, accounting for the tank and its insulation as well as the Phase Change Material (PCM), is calculated considering several factors. The GWP for Glass Fiber Reinforced Polymer (GFRP) and Polyurethane (PUR) is determined from cradle-to-grave, and the vessel, which is assumed to be a perfect sphere with a 14mm GFRP layer, is evaluated using an Environmental Product Declaration (EPD) for GFRP pipes [44].

The production of GFRP pipes, presumed to be similar in GWP to a spherical tank, involves stages like raw material preparation, manufacturing, transportation, installation, and disposal, with the latter using landfill for 25% of the waste as inert filler [44]. Using an average GFRP density of 2500 kg/m3 [45], the GWP per cubic meter is found to be 970.42 kg CO2-eq/m3.

For PUR insulation, another EPD is used, which considers the entire life cycle and indicates a GWP of 541.27 kg CO2-eq/m3 [46]. This encompasses everything from obtaining raw materials to the final product delivery, including transportation, foam application, and disposal, without factoring in recycling benefits.

Both the GWP of GFRP and the PUR can be calculated based on the volume of a spherical shell ($V_h(V)$) as a function of the inner volume of the storage (V) and the known PUR thickness (T).

$$V_{h-GFRP}(V) = \frac{4}{3} \cdot \pi \cdot (\sqrt[3]{\frac{3 \cdot V}{4 \cdot \pi}} + T)^3 - \frac{4}{3} \cdot \pi \cdot (\sqrt[3]{\frac{3 \cdot V}{4 \cdot \pi}})^3 \tag{24}$$

For the GWP of the GFRP, this function can directly be used, with T=0.014m. However, since the PUR is on the outside of the GFRP, the thickness of the GFRP must be added to the inner radius. Adding this to the original Equation 24 gives the new function described in Equation 25.

$$V_{h-PUR}(V) = \frac{4}{3} \cdot \pi \cdot ((\sqrt[3]{\frac{3 \cdot V}{4 \cdot \pi}} + 0.014) + T)^3 - \frac{4}{3} \cdot \pi \cdot (\sqrt[3]{\frac{3 \cdot V}{4 \cdot \pi}} + 0.014)^3 \tag{25}$$

To calculate the complete GWP of the Spherical-Shaped Storage Tank, the earlier mentioned $GWP_{G\text{-}FRP}$ and $GWP_{PUR}$ are multiplied with the corresponding volumes. Both are added together with the $GWP_{Capsules}$, giving the complete function as shown in Equation 26.

$$GWP_{SSST}(V) = GWP_{GFRP} \cdot V_{h-GFRP}(V) + GWP_{PUR} \cdot V_{h-PUR}(V) + GWP_{Capsules}(V) \tag{26}$$

**Repurposed Basement Storage (RBS)**

In the context of Repurposed Basement Storage (RBS), SwissporXPS is utilized as a sophisticated waterproof thermal insulation material, isolating existing basements and unused spaces. This combination of insulation material originates from a previous HSLU-SFOE project, GEAS [18]. To compute the Global Warming Potential (GWP) of this storage type ($GWP_{RBS}$), the GWP of the Extruded Polystyrene (XPS, $GWP_{XPS}$) is combined with the GWP of the encapsulated Phase Change Material (PCM, $GWP_{Capsules}$).

The GWP is identified using the Environmental Product Declaration (EPD) of SwissporXPS [47], which calculates the GWP from the manufacturing phase (up to the factory gate) through to the transport and waste treatment phases at the end of the life cycle, excluding any potential recycling reductions. This results in a GWP of 8.85 kg CO2-eq per kg of XPS. With a stipulated density of 34.3 kg/m³, the GWP per cubic meter ($GWP_{XPS}$) is computed to be 303.56 kg CO2-eq/m³ XPS.

To calculate the GWP ascribed by the XPS, the surface area, where the insulation is applied, must be considered. The basement is presumed to be a cuboid with an unknown base plane and an assumed known height (h). The cuboid surface area, $A_{cuboid}(V)$ is multiplied by the insulation thickness (T) to calculate the quantity of insulation, yielding the volume of used insulation ($V_{XPS}(V)$). Adding $GWP_{Capsules}(V)$ from Equation 27, Equation 28 can be derived.

$$A_{cuboid}(V) = \frac{2 \cdot h^2}{V} + \frac{4 \cdot V}{h} \tag{27}$$

$$GWP_{RBD}(V) = A_{cuboid}(V) \cdot T \cdot GWP_{XPS} + GWP_{Capsules}(V) \tag{28}$$

### 2.4.4 Operational lifetime

This study postulates that, throughout the operational lifetime of the entire system, only the electricity utilized introduces additional Global Warming Potential (GWP) to the system. While the HyTES system chiefly employs solar electricity, it also taps into grid electricity. A study, commissioned by the Federal Office for the Environment, determined that the average GWP of the Swiss electricity grid was 0.128 kg CO2-eq/kWh in 2018, according to the most recent data available from the FOE [33]. Switzerland's electricity, derived from a varied mix of sources from renewables to fossil fuels, experiences significant CO2 emission variations daily and across different days. A study in 2018 indicated that the carbon footprint of electricity could transiently surge to up to five times the annual average [48]. The authors of this study compiled a detailed dataset of Switzerland's hourly CO2 emissions from electricity generation over a year (2015–2016) [49]. Although this data could facilitate a more precise estimate of grid electricity's GWP based on the specific usage pattern, it is beyond the scope of this project. Consequently, the GWP for the operational lifetime is confined to the average GWP per kWh of Swiss grid electricity.

## 2.5 Optimization framework

To determine the optimal configuration for the HyTES system, the NOMAD (Nonlinear Optimization by Mesh Adaptive Direct search) black-box optimizer is employed. NOMAD utilizes simulation-based optimization techniques, making it a viable tool for addressing a variety of optimization challenges. It is particularly beneficial for black-box optimization, where the internal structure of the function is unknown to the optimizer. This characteristic of NOMAD makes it suitable for resource-intensive computer simulations, which often deal with complex, non-smooth, or discontinuous functions that lack easily exploitable properties, such as derivatives.

NOMAD's optimization objective is crafted by employing a function of relevant Key Performance Indicators (KPIs), which are combined into a weighted sum. The KPI functions, expressible as $f_i(x)$, each perform a specific calculation of that KPI, such as Levelized Cost of Heat (LCOH) or carbon footprint (GWP). The specific KPIs utilized in the multi-objective optimization function are delineated in subsection 2.5.1.

The aim is to minimize the value of the multi-objective function while adhering to specified constraints. In mathematical terms, this optimization issue is represented in Equation 29, wherein the optimizer aims to find the minimum value across a defined solution space, denoted as 'Ω'. This space encompasses solutions x that satisfy specific conditions, illustrated in Equation 30. These conditions are defined by constraint functions $c_j(x)$, as indicated in Equation 31, each of which should be less than or equal to zero ($c_j(x) <= 0$). Throughout the HyTES optimization, the constraints are shaped by the ranges of the optimization variables. The functions f(x) and $c_j(x)$ are evaluated via computer simulations to solve the optimization problem.

$$\min_{x\in\Omega} F(x) = (f_1(x), f_2(x), \ldots, f_i(x)) \tag{29}$$

Where the solution space Ω is defined as:

$$\Omega = \{x \in X : c_j(x) \leq 0, j \in J\} \subset \mathbb{R}^n, F, c_j : X \rightarrow \mathbb{R} \cup \{\infty\} \tag{30}$$

Furthermore, j is any number in the set:

$$j \in J = \{1, 2, \ldots, m\} \tag{31}$$

The algorithm optimizes by iteratively generating and refining meshes of varying dimensions, discretizing the design space for efficient exploration. The algorithm evaluates each mesh point representing potential variable values to identify the optimal solution. The algorithm operates in two main stages: "Search" and "Poll". The Search stage enhances the current optimal solution by identifying beneficial mesh locations. The Poll stage generates trial mesh points near the current best solution, underpinning convergence analysis. This robust method allows NOMAD to effectively navigate complex optimization scenarios involving non-smooth, non-convex, or discontinuous functions and uncover optimal solutions.

### 2.5.1 Key performance Indicators

**Levelized Cost of Heat**

The LCOH is a standard KPI used to measure the average cost of generating a unit of energy over the system's lifetime. It considers all costs associated with the system, including construction, operation, maintenance, and grid electricity. In the context of the HyTES project, the LCOH is expressed in Swiss francs per unit of heat ($CHFkWh^{-1}$).

The overall goal of the project is to achieve cost reduction by reducing the component size and volume of a seasonal hybrid heat storage system. In this project, the costs are calculated using the Levelized Cost of Heat (LCOH). For LCOH, the costs refer to the costs of generating and storing heat. The equivalent term for the LCOH is the heat production cost. The LCOH Eq.32 was implemented using the diagram below Fig. 2. [50]

$$LCOH = \frac{CAPEX \cdot ANF + OPEX}{E_{HP,direct} + E_{TES}} \tag{32}$$

The *CAPEX* describes the investment costs (capital investment) and the *OPEX* describes the operating expenses (operational expenses) of the system. The *CAPEX* consists of the following main components and their installation costs: storage, PV system, HP, excavation costs and PCM capsules. The cost functions and sources are discussed further in the next section.

The sum of the energies in the denominator is made up of the energy that is stored and delivered by the TES ($E_{TES}$) and that which is obtained via the HP ( $E_{HP,direct}$) and directly covers the heat requirement. The electrical energy for the HP can come from the grid or from the PV system. The annuity factor (*ANF*) is calculated as follows.

$$ANF_{t,i} = \frac{i\,(1+i)^t}{(1+i)^t - 1} \tag{33}$$

Where $i$ is the interest rate and *t* is the lifespan of the system. The interest rate is chosen in the range of 1-5%. The desired service life of the entire system is 20 years.

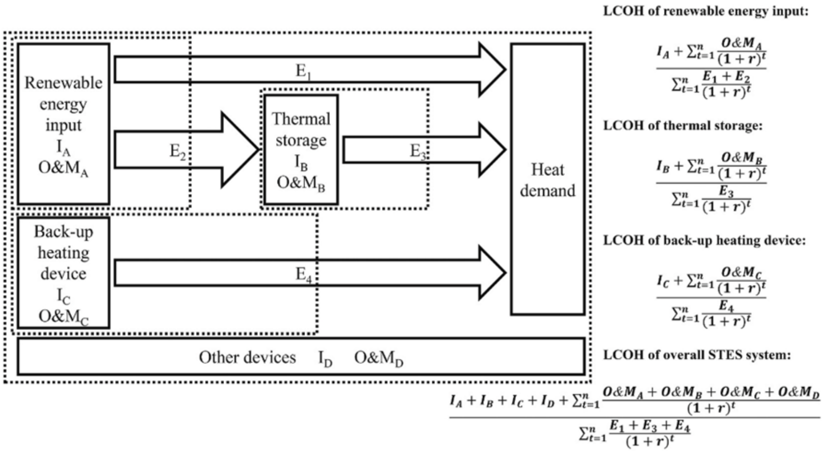

Fig. 2: specific system limits for the calculation of LCOH [50]

### Cost functions to calculate LCOH.

The costs of the different components are estimated using data from various sources. COWA TS directly provided the necessary data for the PCM and encapsulation process and materials. For the GFRS tanks data was directly provided by energy4me as fixed prices including insulation and transport for three sizes. For the VIT concept, the cost function based on Data was taken from Sirch, and used in OPTSAIS was used [4]. The RBS concept costs functions were directly provided by the GEAS project [18], based on the surface and thickness of SwissporXPS materials and water barrier used. The costs for the HWTES were adapted from the Jenni pricelists in OPTSAIS [4] including insulation and installation costs.

With the COVID-19 situation, the PV prices were heavily affected during this transitory period and increased sharply, driven by the cost increases of transportation, polysilicon, and steel. The PV systems cost function developed by Sauter et Al [51] published in 2019 was considered along more updated regressions for the PV costs corresponding to the reports of 2021 and 2022 [52]. Figure 13 shows the comparison of costs using the three mentioned regressions.

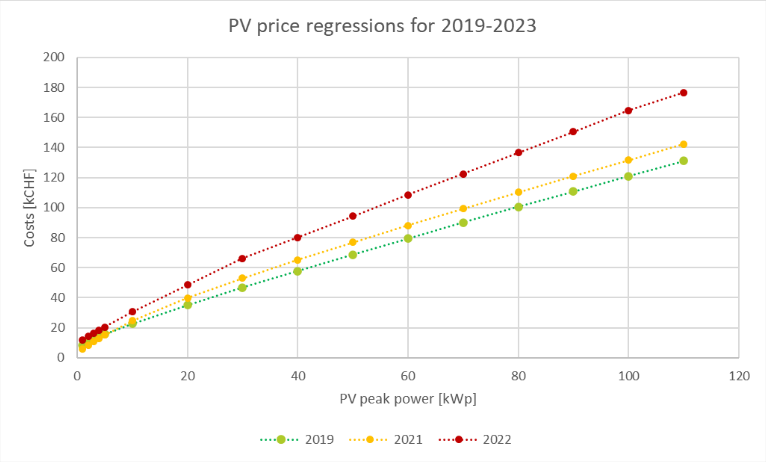

Figure 13 PV price cost functions reported for 2019 [51], 2021 and 2022 [52].

Considering the projections from IEA [53] suggesting the prices tend towards pre-COVID values and should return to a decreasing trend in the next couple of years, the 2019 regression was used for a more realistic projection into the future. For the HP cost function catalog prices from two heat pump manufacturers were used: Price list PL 38 2020, Stiebel Eltron (January 2020) Price list 2021 heat pump system from CTA AG (June 15, 2021).

Table 5 and Table 6 summarize the cost functions and additional information used for the optimization.

| | |
|---|---|
| **Repurposed Basement Storage (RBS)** | $\boldsymbol{I_{TES-GEAS} = (404.56 * L_{Ins} + 80.89) * A_{TES}}$ |
| **Vacuum insulated tank (VIT)** | $I_{TES-VIT} = 7427.4 * {V_{TES}}^{0.5038}$ |
| **Spherical storage tank (SST)** | $I_{TES-SST} = 20548 * {r_{TES}}^2 - 48312 * r_{TES} + 46102 + I_{Ins-GlassWool}$<br>$I_{Ins-GlassWool} = 110 * A_{TES} * L_{Ins}$ |
| **Domestic hot water tank (HWTES)** | $I_{TES-DHW} = 473.95 * r_{TES} + 1873.6 + I_{Ins-GlassWool}$ |
| **PCM and capsules** | $I_{PCM} = C_{PCM} * m_{PCM} + C_{MIX} * V_{PCM} + C_{CapMat} * m_{PCM} + (C_{CapProd} + C_{Filling}) * N_{Cap}$ |
| **Photovoltaics system** | $I_{PV} = \left( \frac{8120}{{PV_{kWp-tot}}^{0.766}} + 1140 * e^{-2.99*10^{-4}*PV_{kWp-tot}} \right) * PV_{kWp-tot}$ |
| **Heat pump** | $I_{HP} = 1167 * HP_{kWth} + 19948$ |

Table 5 Cost function summary.

| | | |
|---|---|---|
| **PCM Costs ($C_{PCM}$)** | 1 | CHF/kg |
| **PCM Costs ($C_{MIX}$)** | 135.63 | CHF/m3 |
| **Capsule Material ($C_{CapMat}$)** | 2.1 | CHF/kg |
| **Capsule production ($C_{CapProd}$)** | 0.0554 | CHF/capsule |
| **Capsule filling ($C_{CapFill}$)** | 0.2 | CHF/capsule |

Table 6 PCM additional material and production costs.

### Thermal self-sufficiency

Thermal self-sufficiency, in this context, is defined as the percentage of energy supplied by the system's PV generation without relying on the external grid. In the case of HyTES, it includes all PV-generated electricity used for heat generation by the heat pump. Excess PV electricity fed back to the grid is excluded. Self-sufficiency can be calculated by dividing the heat generated with PV electricity by the total heat demand.

Increasing self-sufficiency requires increasing the capacity variables, such as PV panels and storage capacity, most likely resulting in higher system cost and carbon footprint. However, by decreasing grid electricity usage, associated costs, and the carbon footprint of grid electricity can be mitigated.

### Global warming potential

To meet the project's aim of lowering Switzerland's carbon footprint, the system's Greenhouse Gas Emissions (GHGE) are crucial and should be minimized in the optimization process. GHGE includes various gases, like CO2 and methane, which can be measured together using Global Warming Potential (GWP), expressed in kg CO2-equivalent (CO2-eq). GWP helps compare the environmental impact of different technologies and assess sustainability, with details on estimating the system's GWP provided in Section 5.

To compare with the Levelized Cost of Heat (LCOH), the carbon footprint can also be expressed in monetary terms through carbon pricing, a method that assigns a cost to GHGE, encouraging reduction efforts [54]. Switzerland's government prices carbon at 120 Swiss Francs (CHF) per ton of CO2, which can be used to convert the system's GWP into financial terms. For complete alignment with LCOH, the GWP in CHF should also be divided by the total generated heat, allowing measurement in the same unit (CHF $kWh^{-1}$).

### 2.5.2 Objective function

Weighting plays a crucial role in multi-objective optimization functions as it allows the expression of preferences and priorities among competing objectives. Assigning weights depends heavily on the client's preferences [35].

To accommodate the NOMAD optimizers' requirement of a single-function problem, the weighted sum method is used, which represents multiple objectives as a single function. The single objective function is constructed by summing objective functions $f_i$ multiplied by weighting coefficients $w_i$, as shown in Equation 34.

$$\min_{x \in \Omega} F(x) = \sum_{i=1}^{j} w_i \cdot f_i(x) \tag{34}$$

$$w_i \geq 0, \forall i = 1, \ldots, j \text{ and } \sum_{i=1}^{j} w_i = 1 \tag{35}$$

Weights are assigned based on the decision-maker's knowledge of the problem. However, a weighting factor should also contain normalization to ensure fair consideration. Where $p_i$ represents the assigned weights and $\theta_i$ denotes the normalization factors [55].

$$w_i = p_i \cdot \theta_i \tag{36}$$

### Weighting factors

The weighting factors ($p_i$) steer the optimization towards a particular desired outcome. As mentioned earlier, the desired outcomes mainly revolve around $SS_{th}$ (between 70% and 100%). To set up the optimization function for various levels of $SS_{th}$, a total weighting factor of 1 (100%) can be divided over weighting factors for the KPIs. By putting a more significant emphasis on the SS, by increasing the SS weighting factor '$p_{SS}$', the optimization results in higher levels of self-sufficiency.

Determining the appropriate weighting factors in advance is unrealistic, so a parameter sweep of $p_{SS}$ is necessary to find the suitable pareto front optimal solution set that covers most of the range. Regarding the optimization goals for LCOH and GWP, the weighting factors are denoted as $p_{LCOH}$ and $p_{GWP}$, respectively. The remaining weighting value is evenly split between these two objectives, as shown in Eq. 37 and Eq. 38. This distribution is considered fair since both objectives are expressed in the same unit, and the normalization factors, $\theta_i$, equalize their magnitudes (explained in the following subsection).

$$p_{LCOH} = \frac{(1 - p_{SS})}{2} \tag{37}$$

$$p_{GWP} = \frac{(1 - p_{SS})}{2} \tag{38}$$

### Normalization factors

The normalization method described by O. Grodzevich et al. determines the normalization factor, adjusted for this specific optimization [55]. The method exploits variances in optimal function values to define optimization boundaries by identifying two key points within the solution set: the Utopia and Nadir points. The Utopia point (U) represents the theoretical best value for each objective. Its components ($z^U_i$) are calculated using Eq. 39, which determines the optimal solution for each objective function (fi). While the Utopia point is often unattainable due to conflicting objectives, it provides the lower bounds of the Pareto optimal set.

$$z_i^U = \min_x f_i(x) : x \in \Omega \tag{39}$$

Conversely, the Nadir point (N) represents the least favorable outcome for each objective. Its components ($z^N_i$) are calculated using Eq. 40, which finds the maximum values of the objective functions.

$$z_i^N = \max_x f_i(x) : x \in \Omega \tag{40}$$

To find this project's Utopia and Nadir points, the NOMAD optimizer is executed three times, using Eq. 41. With $p_{LCOH}$ = 1, the optimization finds the lowest LCOH and its corresponding GWP and SS. Similarly, with $p_{GWP} = 1$, the optimization identifies the minimum GWP and its corresponding LCOH and SS. Finally, it is run for $p_{SS} = 1$, which finds the highest SS and the corresponding other values.

$$\begin{gathered}\min_{x \in \Omega} F(x) = p_{LCOH} \cdot f_{LCOH} + p_{GWP} \cdot f_{GWP} + (1 - p_S) \cdot f_{SS} \\ \text{for:} \\ p_{LCOH} = 1, p_{GWP} = 0, p_{SS} = 0 \\ p_{LCOH} = 0, p_{GWP} = 1, p_{SS} = 0 \\ p_{LCOH} = 0, p_{GWP} = 0, p_{SS} = 1\end{gathered} \tag{41}$$

Figure 14 shows an example of the utopia and nadir points calculated for the VIT concept.

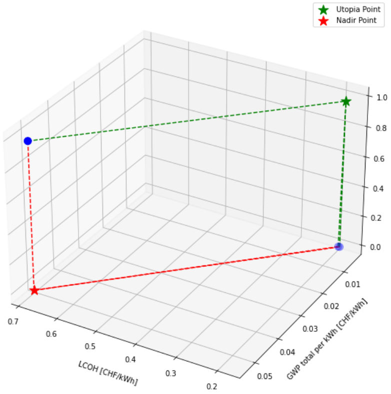

Figure 14 Example of Nadir and Utopia points for VIT concept.

The normalizing method leverages the differences in optimal function values between the Nadir and Utopia points to calculate the normalization factor $\theta_i$ using Eq. 42. This normalization scheme ensures optimal normalization results, bounding objective function values between 0 and 1 (see Eq. 43).

$$\theta_i = \frac{1}{z_i^N - z_i^U} \tag{42}$$

$$0 \leq \frac{f_i(x) - z_i^N}{z_i^N - z_i^U} \leq 1 \tag{43}$$

Computing normalization weights is a process that involves solving optimization problems to secure specific values. This task, though, can be computationally demanding, especially when dealing with more intricate problem types. Nevertheless, finding exact solutions for each optimization problem is only sometimes a necessity [55]. Knowing the estimates of Utopia and Nadir points makes it possible to derive suitable normalization factors. Modifications and relaxations can be utilized to counter the computational burdens. For instance, the parameters of the optimization solver can be adjusted, like enlarging tolerances or duality gap criteria, to decrease the time taken for solutions.
Another method, called ’relaxing constraints’, can also be used to ease the computational load. This involves loosening or eliminating ’hard’ constraints.

### Complete optimization objective

The complete optimization function integrates the KPIs, weighting factors, and normalization into a single objective function. This function, denoted as F(x), represents the objective to be minimized during the optimization process. The function is expressed as Equation 44.

$$\min_{x\in\Omega} F(x) = \frac{(1-p_{SS})}{2} \cdot \theta_{LCOH} \cdot f_{LCOH} + \frac{(1-p_{SS})}{2} \cdot \theta_{GWP} \cdot f_{GWP} + p_{SS} \cdot (1-f_{SS}) \tag{44}$$

The optimization Equation 44 encapsulates the multi-objective nature of the problem, providing a comprehensive representation of the objectives and their relative importance. The NOMAD optimizer uses this function to iteratively search for the optimal solution that minimizes the overall objective, considering the trade-offs between LCOH, GWP, and self-sufficiency.

### 2.5.3 Optimization variables

The optimization process involves a variety of variables, each influencing the system's overall performance. These variables are adjusted through an iterative process until the optimizer determines the system configuration that optimally satisfies the multi-objective function.
As described in section 2, the model used for simulation is extensive and uses numerous input parameters to thoroughly describe the system. Due to the sheer number of these parameters, most of them had to be fixed based on assumptions and existing specifications for component performance as well as any additional specifications, lifetime, financial parameters, and building-related parameters.

To maintain a realistic optimization process, in terms of computational power, given that optimization run time tends to increase with the number of variables exponentially, the number of variables was reduced as much as possible, while retaining the key aspect of the system to be optimized. These include the storage units' sizes, capsule shape, size, and phase change temperature within the capsules, in addition to the PV peak power and orientation, and the maximum HP power:

- SHTES tank type
- SHTES size (Height, Diameter)
- PCM packed bed section size (Middle position, Thickness)
- PCM capsule size
- PCM capsule shape
- PCM type
- DHWTES size (Height, Diameter)
- Amount of PV panels
- PV orientation (Azimuth and Tilt)
- HP power (Electrical)

### SHTES Tank

Variables associated with the HyTES tank itself consist of the specific type and its dimensions (height and diameter). First, the different tank types, varying in material, shape, and implementation, can yield different operational results. This is because of energy losses, PCM capsule packing density, tank costs and GWP depend on the storage tank type.

Further, the tank's dimensions significantly impact the thermal energy storage for space heating and preheating domestic hot water while also influencing the degree of heat losses. The burial depth mainly limits the optimization range for the dimensions of the HyTES. The burial depth and thus the height of the reservoir is limited to 4 m because, from this depth, the burial costs rise disproportionately [4].

### PCM capsules packed bed section.

The PCM capsules packed bed in the HyTES tank can also be varied. This is done by changing at which vertical level of the HyTES tank the packed bed starts from the bottom, which in turn determines the thickness of the packed bed layer.

The capsule shapes defined as the domain for this parameter were discretized into four options, selected arbitrarily due to the spread of characteristics in terms of both surface to volume ratio and packing density. The chosen geometries are Spheres, Cylinders of aspect ratio 2.5, Ellipsoids of aspect ratio 2.5 and the current COWA booster capsule geometry for domestic hot water applications.

The mathematical description of the geometry using the super ellipsoid model allowed the iterative determination of the capsule surface to volume ratio, key input parameter for an accurate hollow sphere approximation for varying sizes, in the range of 100mL to 5L as seen in Figure 15. Additionally, a polynomial regression was applied to easily recalculate the surface for each type of capsule based on the set capsule volume.

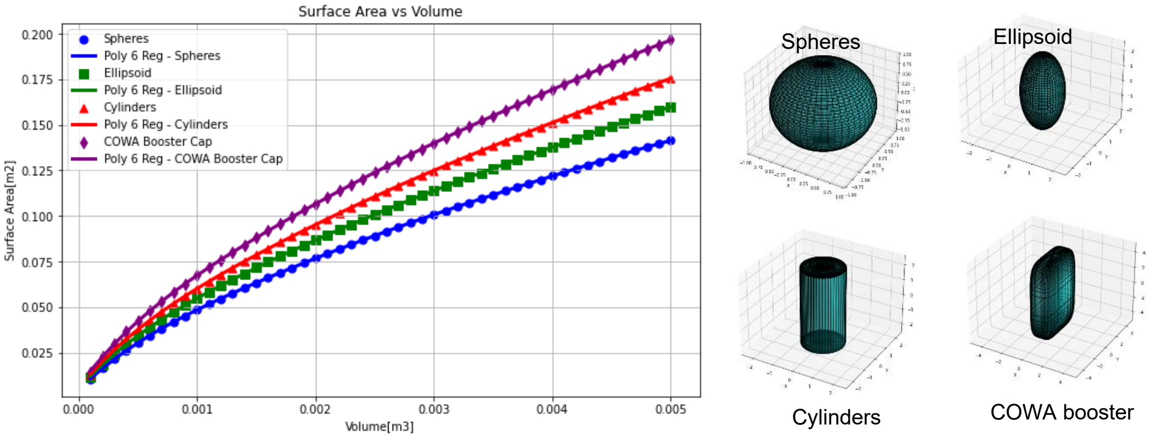

Figure 15 Surface vs volume plot for the individual capsule shapes considered in the optimization domain.

The interaction between capsule shape and container defines the border effects over the packed bed structure. To get a more accurate estimate of the packing density in the different scenarios, COWA booster capsules were used as input in rigid body simulations of the packing process. The simulations allowed to estimate the packing density of the capsules arranged randomly in the three types of storage tanks for 135mL capsules in 1m3 containers. Considering a small container of 1 m3 (in the scale of the optimization domain) allows a realistic estimate due to the high border effects present. These effects are mitigated for larger containers and larger number of capsules and the packing density is expected to remain the same or marginally improve at those scales. A sample of the simulated structures can be seen below for the COWA booster caps geometry.

Figure 16 Picture of simulated packed bed configurations for the three container shapes.

Taking as blueprint the scaling factors between the three container shapes and the COWA booster caps, simpler simulations for each one of the other capsule geometries were conducted in cylindrical containers only at low diameter ratios to match similar, high border effects. These estimates were then scaled using the same ratios found for the actual simulations with the COWA booster capsules in the three container geometries.

The summary of these results, and the actual values used within the simulations and optimization can be found in Table 7.

| **Packing Density [%]** | **Cylinder** | **Cuboid** | **Sphere** |
|---|---|---|---|
| **Sphere caps** | 60.3 | 60.1 | 57.3 |
| Ellipsoid caps | 62.5 | 62.1 | 59.8 |
| Cylinder caps | 59.3 | 59.2 | 56.9 |
| COWA Booster caps | 62.6 | 62.2 | 61.1 |

Table 7 Packing densities for the different capsule shapes in the corresponding container geometries.

**DHW TES**

The optimal DHW TES size can significantly influence the total needed HP power, as the peak DHW demand can be fully supplied from the DHW TES if sized correctly. Besides the peak demand, a smaller DHW TES might lead to a more significant reliance on the heat pump (preheated by the HyTES tank) during low solar power periods, requiring grid electricity.

For the range of the DHW TES, the average DHW consumption and the product catalogue of a DHW TES supplier are used. In Switzerland the average DHW consumption per resident is about 50 l of hot water at 60 °C per day [14]. Considering the reference building has 20 residents an estimate of 1 $m^3$ of DHW of 60°C combined. According to the product overview of Sirch, this translates to a tank with a height of 2 m and a diameter of 0.8 m [56].

However, it is more likely that the tank needs to be more significant because the consumption and charge profiles might not be in optimal relation. Besides that, as the DHW is discharged, the temperature can decrease, requiring more water than the exact amount.
As the DHW TES in the HyTES system is coupled with the HyTES tank, it is also possible that the optimal size might be slightly less. Therefore, the ranges of the DHW TES are assumed to be the same

as the ranges of the standard DHW TES tanks of Sirch. The minimal tank is 0.5 $m^3$ or (h x d) 2 x 0.5 m, and the maximum size tank is 5 $m^3$ or 2.5 x 1.6 m.

### PV system

The optimization variables for the Photovoltaic (PV) system include the number of panels and their orientation, both in Azimuth (horizontal angle, $\phi$) and tilt (vertical angle, $\alpha$). While increasing the number of panels enhances energy self-sufficiency by converting more solar energy to electricity, it also raises the system's cost and Global Warming Potential (GWP), requiring a balanced approach.

The panel orientation is vital to maximize solar energy capture, with optimal orientations varying based on location, climate conditions, and solar path. The building used for the HyTES project, specified in the OPTSAIS project, and analyzed based on information from the Swiss Federal Statistical Office and building guidelines from the Bern and Zurich cantons, is considered to have a flat roof, allowing adjustments in Azimuth and tilt [8]. The average building is stated to have a total available roof area of 264 m2, determining the maximum number of panels (MaxPV). Additionally based on the study performed by Anderegg et Al. [57] that total roof area only 66% is usable for PV installations.

### Heat pump.

The possible optimization variables of the air source heat pump are reduced to the max electrical power in the model, indirectly dictating the maximum heat output (together with the internally calculated COP). By varying the electrical power, the model sizes the heat pump on all fronts, influencing factors like cost, GWP, and ability to charge the HyTES tank. Thus, the selected electrical power level affects the system's overall operation.

The range of the electric power of the HP is assumed to be from 16 kWth to 100 kWth. This range is well within the maximum range of available air source heat pumps. The heat pump can modulate its power in a range of 25-100% of the maximum electrical power set.

### Overview of optimization variables:

In Table 8, all the variables and the corresponding ranges are summarized.

| Properties | Lower bound | Upper bound |
|---|---|---|
| **SHTES tank height [m]** | 1 | 3 |
| **SHTES tank width[m]** | 1 | 4 |
| **PCM packed bed relative height [-]** | 0.1 | 0.9 |
| **PCM Capsule Size [ml]** | 135 | 5000 |
| **DHW tank height [m]** | 2 | 2.5 |
| **DHW tank width [m]** | 0.5 | 1.8 |
| **Amount of PV panels [-]** | 0 | 95 |
| **PV Azimuth angle [°]** | 90 | 270 |
| **PV Tilt angle [°]** | 0 | 45 |
| **Electrical power HP [kW]** | 4 | 40 |

Table 8 Overview of the ranges for the optimization variables

### 2.5.4 Base case

To provide better insights into the meaning of the values of LCOH and GWP, it is essential to establish a reference point by comparing these values to a base case. Considering that fossil fuels, mainly fuel oil, are predominantly utilized for heating in multi-family houses, the base case involves comparing the HyTES system against using fuel oil boilers [58].

**Levelized Cost of Heat of an oil boiler.**

An extensive study was performed by M.J.S. Zuberi et al. (2021) about the potential cost of various heating systems in Switzerland's residential areas [59]. Their study showed that the LCOH of different heating technologies for MFH hardly differed throughout the cantons. In Figure 10, they presented an overview of the different investigated heating technologies in MFH in Switzerland for three different residential areas: urban, suburban, and rural. Figure 17 shows the LCOH of an oil boiler to be 0.14 CHF kWh−1 for an MFH in an urban area. This study assumed an operational lifetime for the boiler of 20 years. It also must be noted that this study did not consider the projected increase in oil prices. Therefore, the LCOH of 0.14 CHF kWh$^{-1}$ could be considered a best-case scenario.

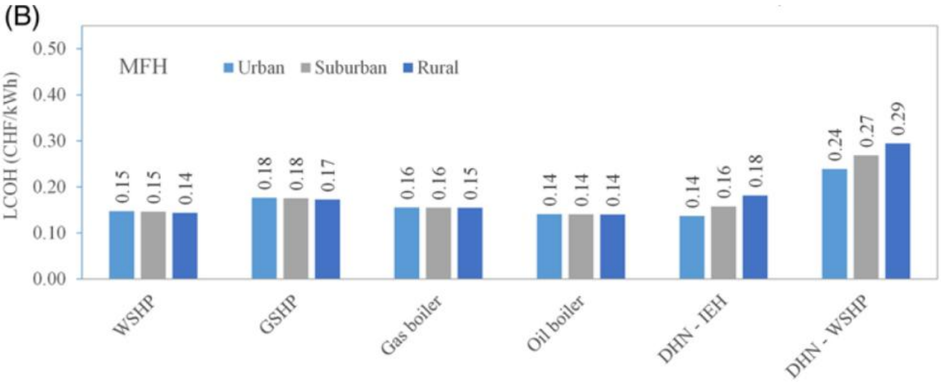

Figure 17 Levelized Costs of Heat for different heating technologies in multi-family houses in Switzerland (WSHP = Water Source HP, SHP = Ground Source HP, DHN = District Heating Network and IEH = Industrial Excess Heat) [42].

**Global Warming Potential of an oil boiler**

To calculate the GWP of an oil boiler, it is assumed that the GWP induced by the boiler itself is negligible compared to the GWP from the fuel. According to the Federal Office for the Environment, the emission factor of Light fuel oil used in oil boilers is 0.265 kg $CO_{2\text{-eq}}$kWh$^{-1}$[60]). This value must be adjusted for the efficiency of an oil boiler. M.J.S. Zuberi et al. (2021) specified the average efficiency of an oil boiler to be 83% [59].

Finally, as the preferred unit in this optimization is CHF kWh$^{-1}$, to align with LCOH, the emission factor need to be multiplied by the carbon price of CHF 120 per ton of CO2. Equation 49. shows that the final GWP of an oil boiler ($GWP_{OB}$) is 0.03831 CHF kWh$^{-1}$.

$$GWP_{OB} = \frac{0.265}{0.83} * 0.120 = 0.03831 \;\; CHF\,\mathrm{kWh}^{-1} \qquad (49)$$

# 3 Results and discussion

The validations of the models and initial simulation results are shown below.

## 3.1 Validation

### 3.1.1 Validation of the PV model

The PV model was created using the commercial validated software PV*SOL [61]. This is a program for the design and optimization of photovoltaic systems in combination with consumers, battery systems and electric vehicles. It was used to create a reference model, which was re-simulated with the PV model. The electrical energy produced was added up and compared with each other. The validation parameters used can be found below in Table 9.

| **Location** | **Basel-Binningen** |
|---|---|
| **Weather data** | Meteonorm Climate Date (1991-2010) |
| **PV module** | JAP72S03-340/SC (JA Solar Holdings Co., Ltd) |
| **PV area** | 26.7 m2 |
| **Alignment angle** | 180° (southern orientation) |
| **Angle of inclination** | 30° |

Table 9 Overview of the parameters used to validate the PV model.

One year was simulated, starting on January 1st. Equation 12 was used to calculate the power of the PV modules, with the parameters chosen based on the data sheet of the solar modules under consideration. In addition, an efficiency of the PV system of 96% was assumed.

The deviation of the two summed solar yields is approx. 0.3%, whereby the summed electrical energy of the self-created model is greater than that of the reference model. When monthly solar yields are compared, the largest deviation is 1.4% in December, which corresponds to an absolute deviation of 2.8 kWh. The largest absolute deviation is reached in June, at 8 kWh (1%). The total yield over the year is 6409 kWh for this system and this location.

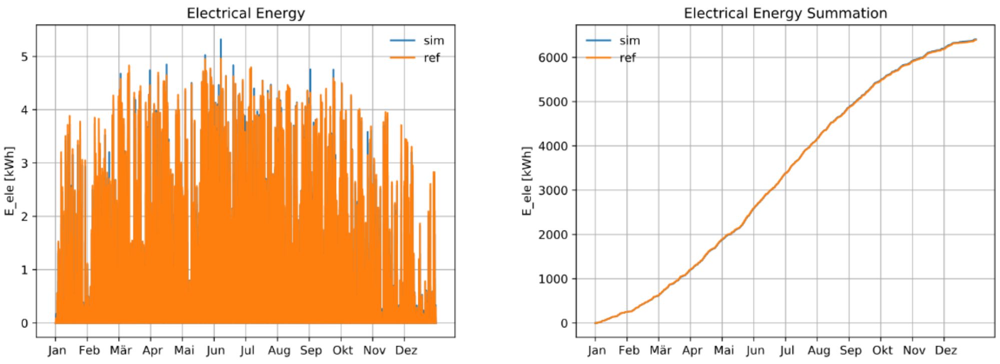

Figure 18 Validation of the PV model using PV-sol.

### 3.1.2 Validation of heat requirements

The heating requirement profile was validated and checked for plausibility using an energy balance. For this purpose, demand profiles were created using the “Heating Degree Hour” methodology for different flow temperatures at various locations. The heat demand profiles created in this way with an hourly resolution were summed up and compared with the corresponding heating demand for a year (area-specific heating demand and heated area). No deviations could be found. It was also successfully verified that the simulation follows the heat demand profile created.

### 3.1.3 Validation PCM sphere model

To validate the PCM spherical model, measurements were conducted on a prototype from Cowa, built at HSLU's Thermal Energy Storage Competence Center. The prototype consists of three main components, namely: the heat pump (1), the buffer tank (2), and the underfloor heating mixing group (3), as shown below. The prototype and its components are described in more detail below.

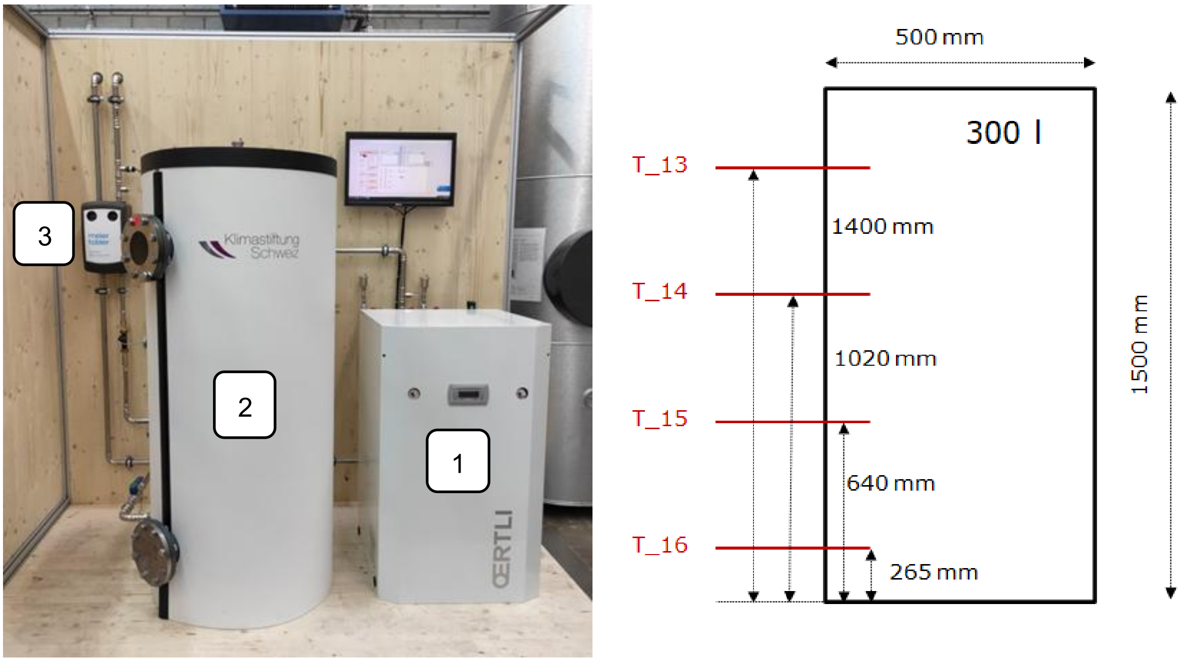

Figure 19 Left: Prototype with the heat pump (1), the buffer storage (2), and the underfloor heating mixing group (3); Right: Detailed sketch of the buffer storage with the four temperature sensors distributed over the height.

The buffer tank has a filling volume of 300 L. This was filled by hand with PCM capsules via the upper flange. In total, the storage could be filled with 2,518 capsules. This results in a packing density of 63.2%.

**Scheme and data acquisition.**

The test stand was designed so that the entire prototype can be charged and discharged under conditions that are as realistic as possible. The test stand consists of three measuring circuits, namely: (1) the heat pump circuit for loading the storage, (2) the floor heating circuit for discharging the storage and (3) the buffer storage itself. The diagram of the test stand can be seen in Figure 20

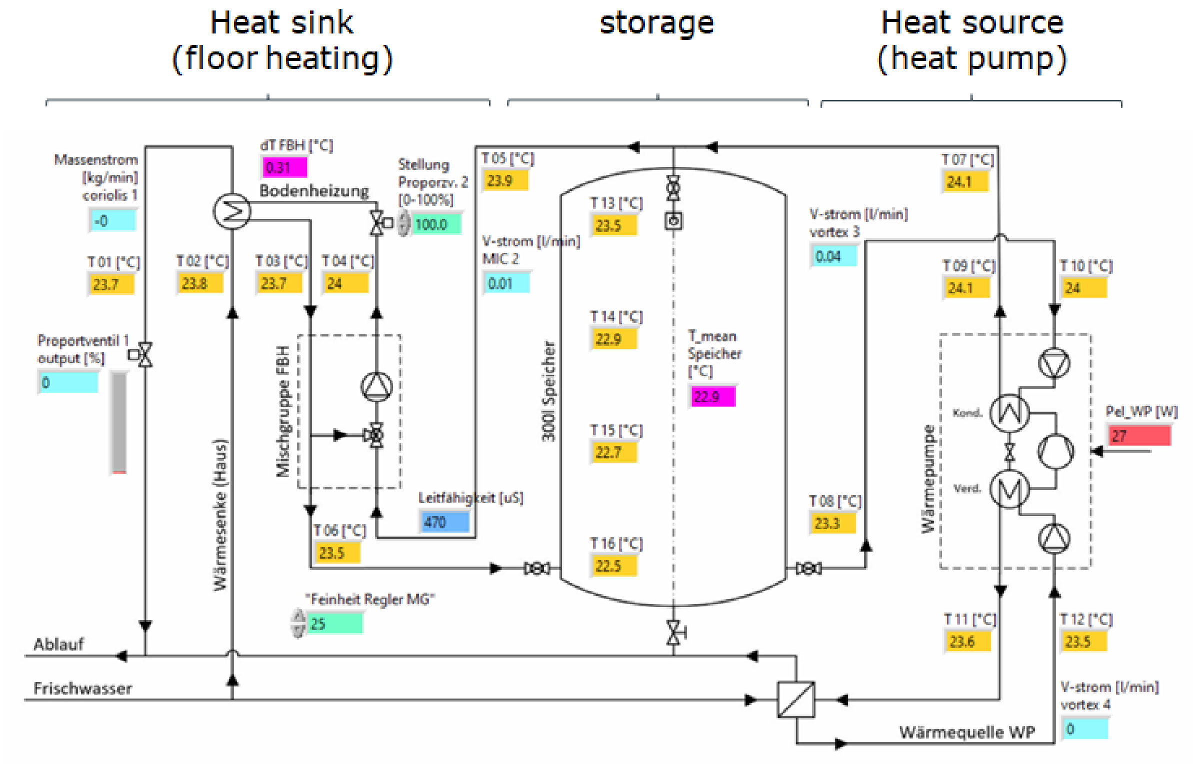

Figure 20 Scheme of the test bench/prototype from COWA TS

The temperature and the volume flow were measured at various points. The following table provides an overview of the sensor technology:

| Designation | Measuring point | Measuring circuit |
|---|---|---|
| **T01** | Heat sink return temperature | Floor heating |
| **T02** | Flow temperature of the heat sink | Floor heating |
| **T03** | Return (pre-mix) | Floor heating |
| **T04** | Flow (post-mix) | Floor heating |
| **T05** | Buffer → floor flow | Buffer |
| **T06** | Floor → buffer return | Buffer |
| **T07** | HP → buffer flow | Buffer |
| **T08** | Buffer → HP return | Buffer |
| **T09-T12** | Cond./Evap. inlet/outlet | Heat pump |
| **T13-T16** | Temps. at buffer levels | Buffer |
| **Coriolis 1** | Flow (floor heating) | Floor heating |
| **Vol. flow MIC 2** | Buffer → floor flow | Buffer |
| **Vortex flow 3** | Volume flow heat pump circuit into the buffer storage | Buffer |
| **Vortex flow 4** | Volume flow heat source for the heat pump | Heat pump |
| **P $_{El}$ WP** | Electrical power heat pump | Heat pump |
| **conductivity** | Water quality/salt leak detector | Buffer |

Table 10 Overview of installed sensors on the test bench.

A charging and discharging process are shown below for the qualitative validation of the model. For the quantitative validation, 5 experiments were used, in which different mass flows were also used. It was shown that the errors in the energy quantities are always less than 10% when comparing simulation and experiment (see Figure 21 to Figure 24).

### Charging process

In Figure 21 and Figure 22 the course of the storage temperatures (T13 - T16), respectively the charging power and the energy stored in the buffer storage over the entire charging period can be seen in comparison to the simulation results (dashed lines). During the charging process, the storage tank was heated from an average temperature of 21°C to approx. 40°C using the heat pump. In terms of quality, the temperature curve in the storage corresponds well and the amount of energy stored is accurate enough that the error in annual simulations is negligible. When looking at the charging power, it becomes clear that the temporal agreement could be improved, but it should be noted that the average power agrees well, which is crucial in the annual simulations.

The amount of energy stored in the charging experiment is 13.1 kWh, which corresponds to a deviation of 5.1% compared to the simulation of 12.5 kWh. This is considered sufficiently accurate, especially considering that in HyTES relative comparisons of system sizes and variables are of greater interest than precise predictions of the absolute performance of systems.

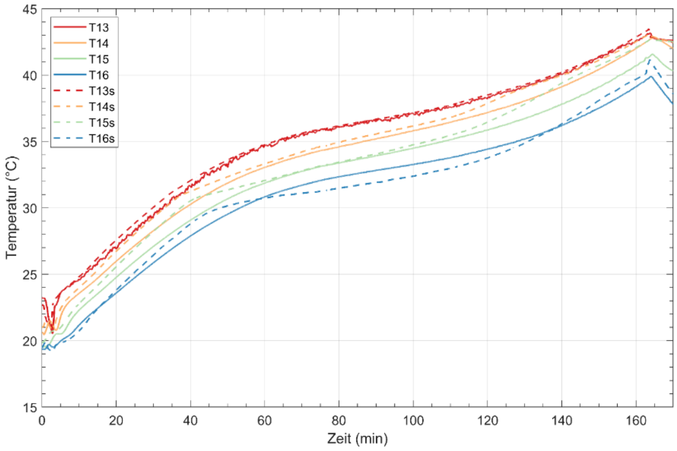

Figure 21 Temperatures T13 to T14 (positions as shown in Figure 20) over the charging cycle for the experiment and the simulation (s).

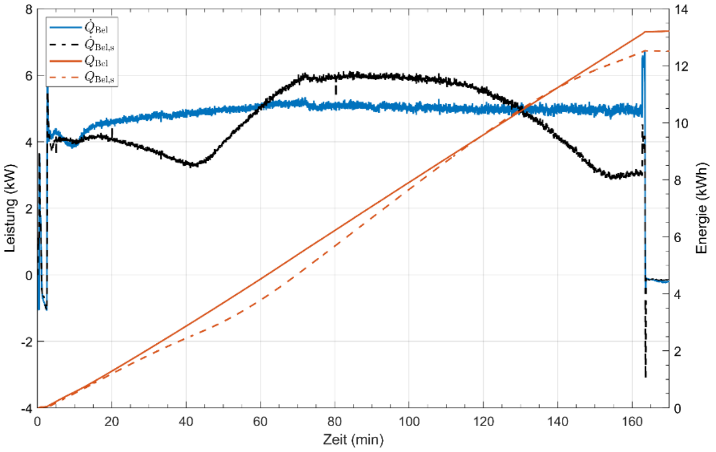

Figure 22 Power and integrated energy stored in the buffer over the charging time, with (s) for the simulation.

## Discharging process

In Figure 23 and Figure 24, the course of the storage temperatures (T13 - T16), respectively the discharge power and the energy released from the buffer storage over the entire discharging period can be seen in comparison to the simulation results (dashed lines). During the discharging process, the storage tank was discharged from an average temperature of 40°C to approx. 20°C via the emulated floor heating. In terms of quality, the temperature curve in the storage corresponds relatively well and the amount of energy stored is also sufficiently accurate for annual simulations.

The amount of energy that was stored in the discharging experiment is 13.1 kWh, which corresponds to a deviation of approx. 6% compared to the simulation of 14.0 kWh. This is considered sufficiently accurate, especially considering that in HyTES relative comparisons of system sizes and variables are of greater interest than precise predictions of the absolute performance of systems.

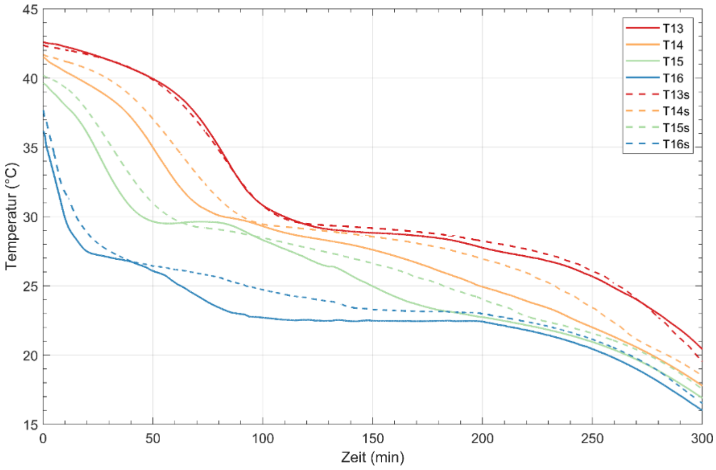

Figure 23 Temperatures T 13 to T 14 (positions as shown in Figure 20) over the discharge cycle for the experiment and simulation (s).

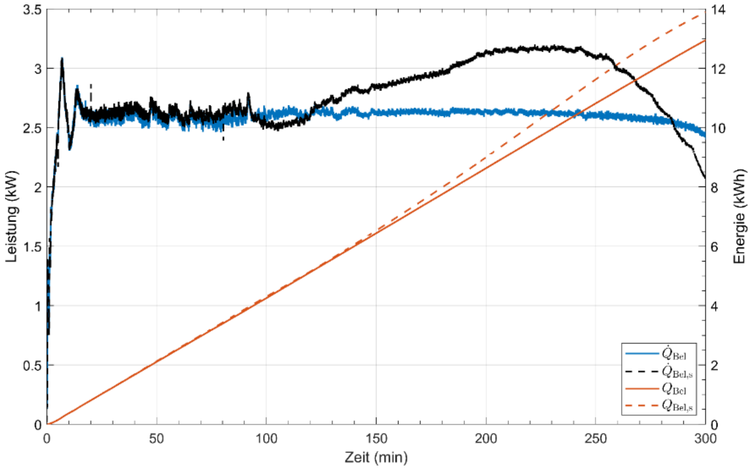

Figure 24 Power and integrated energy stored in the buffer over the discharge period, with (s) for the simulation.

### 3.1.4 Validation of the WP model

The heat pump model was validated with data from a prototype from Cowa. The Prototype consists of a heat pump, a buffer storage, and a heat sink. Further information about the test bench can be found in Section 3.1.3. The following measuring points on the test bench were used for the validation (a diagram of the test bench can be seen in Figure 19): water-side inlet and outlet temperatures at the condenser and evaporator, the electrical power drawn from the HP and the water-side mass flows. Based on these measurement data, the thermal energy produced was determined using the model and compared with the experimental measurement data. The deviation of approx. 2%. is mainly due to the measurement inaccuracy of the measured electrical power of the heat pump.

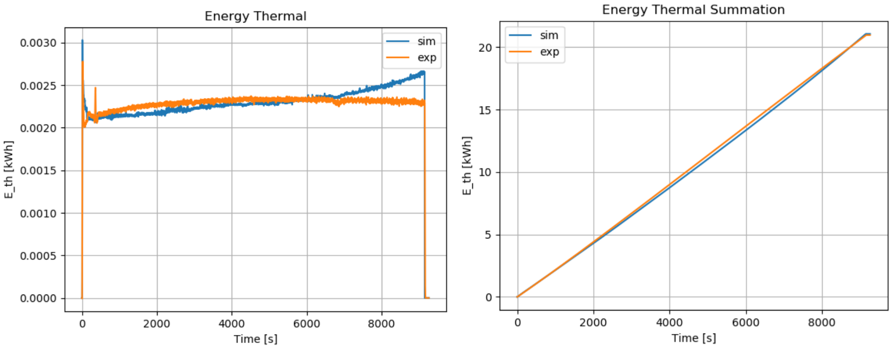

## 3.2 Overview and discussion of model outputs.

### 3.2.1 Performance comparison between hybrid and sensible SHTES.

In this section, the main outputs of our model are presented and discussed, focusing on the comparison between fully sensible systems and hybrid systems incorporating PCM. The comparison covers performance, costs, and global warming potential. Table 11 summarizes the system inputs for both configurations using the RBS concept.

| | **Sensible SHTES** | **Hybrid SHTES** |
|---|---|---|
| **PV Power [kWp]** | 36.1 | 36.1 |
| **PV Azimuth [deg]** | 180 | 180 |
| **PV Tilt [deg]** | 45 | 45 |
| **HP power [kWe]** | 23 | 23 |
| **SHTES Volume [m3]** | 9.24 | 9.24 |
| **SHTES Height [m]** | 3 | 3 |
| **SHTES Diameter [m]** | 1.76 | 1.76 |
| **Total number of capsules [-]** | - | 2655 |
| Capsule volume [L] | - | 2 |
| Capsule type [-] | - | COWA booster |
| PCM type [-] | - | PCM – 1 |
| **Total PCM mass [kg]** | - | 6335 |
| **Total PCM volume [m3]** | - | 4.9 |
| **Total Capsule mass [kg]** | - | 402 |
| **HWTES Volume [m3]** | 1.85 | 1.85 |
| **HWTES Height [m]** | 1.5 | 1.5 |
| **HWTES Diameter [m]** | 1.25 | 1.25 |

Table 11 Summary of inputs for example RBS system.

For the fully sensible system, the steady state temperature distribution and evolution over the year, at 5 different heights (T1 to T5 from the bottom) is displayed in Figure 25, along with the state of charge of the storage over the year.

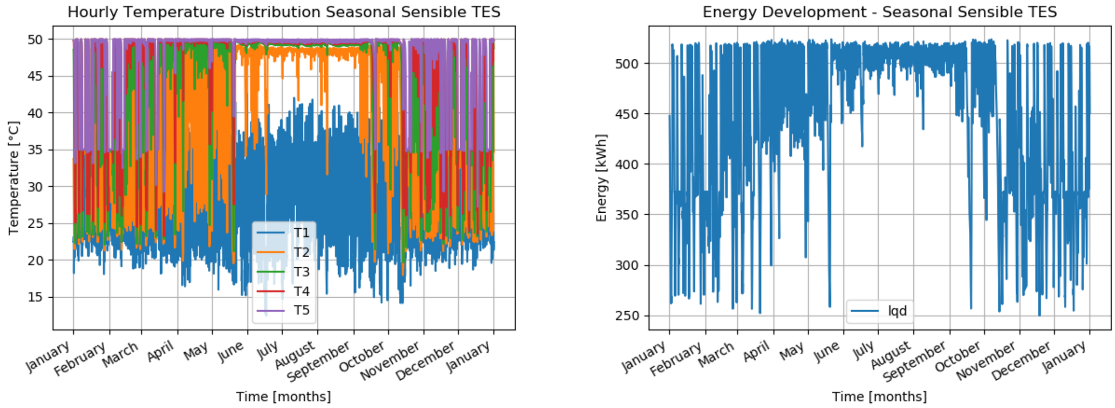

Figure 25 Yearly temperature distribution and stored energy in fully sensible SHTES for example RBS system.

The storage system operates up to full charge from March to October, indicating heavy use during these months. Even during the summer, the SHTES operates constantly due to its coupling with HWTES through water preheating in HEX1, functioning as a medium-term storage, and maintaining some capacity during winter. The sensible system experiences large temperature swings and full charge-discharge cycles, highlighting its dynamic operation.

In the hybrid system, the PCM occupies 90% of the storage height with a volume share of 52% in the SHTES. Unlike the fully sensible system, the temperatures around the PCM section (T1 to T5) tend to stabilize around the phase change temperature (40°C) throughout the year. This stabilization is graphically evident as the PCM dampens extreme temperature fluctuations, providing a more consistent temperature profile even during heavy load periods and winter discharge. Figure 26 presents the temperature distribution and energy development in the tank with a PCM capsule packed bed section.

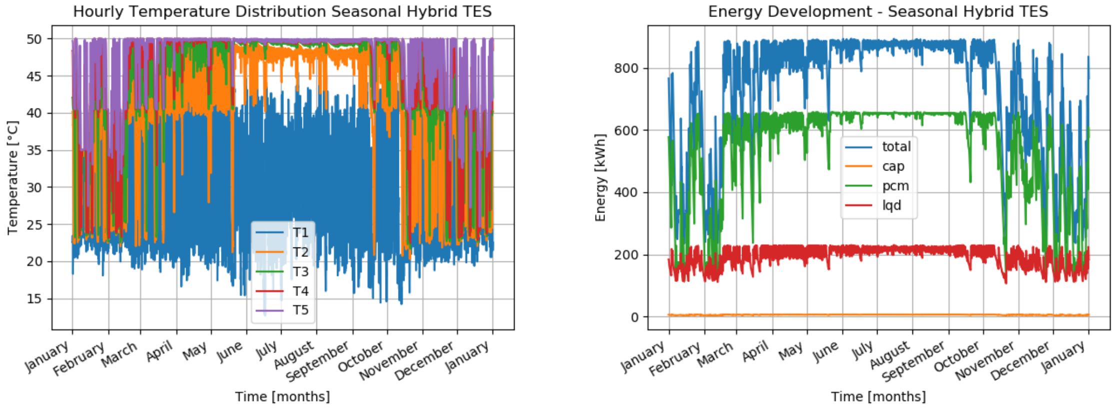

Figure 26 Yearly temperature distribution and stored energy in hybrid sensible and latent SHTES for example RBS system.

The addition of PCM capsules increased the total capacity of the SHTES by approximately 1.7 times compared to the sensible system. This increase, coupled with temperature stabilization, enhances the system's self-consumption by about 2% and overall self-sufficiency by about 4.7%.

Figure 27 shows the Sankey diagram of energy flows in the hybrid system. The SHTES supplies 60-70% of the domestic hot water (DHW) demand, reducing heat pump load and maximizing the utilization of excess PV energy.

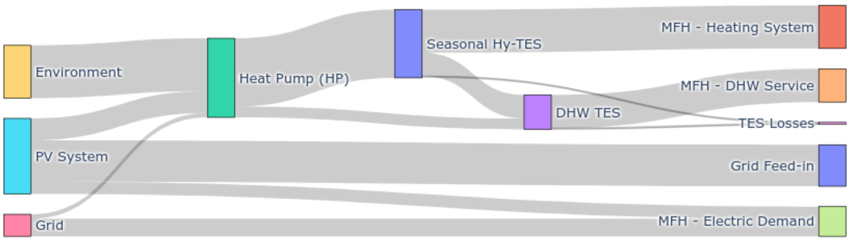

Figure 27 Sankey diagram of yearly energy flows for the hybrid SHTES RBS example.

Table 12 compares the KPIs of the fully sensible and hybrid systems. The hybrid system achieves higher self-sufficiency at a higher cost and GWP due to PCM costs and manufacturing processes.

| | **Sensible SHTES** | **Hybrid SHTES** |
|---|---|---|
| **Self-Sufficiency Thermal [%]** | 79.9 | 84.6 |
| **LCOH [CHF/kWh]** | 0.325 | 0.334 |
| **GWP [CHF/kWh]** | 9.95E-03 | 1.18E-02 |
| **Self-Sufficiency Electric [%]** | 39.9 | 40.4 |
| **PV Self-Consumption [%]** | 42.5 | 44.2 |
| **Comfort level [%]** | 99.1 | 99.1 |

Table 12 Summary of KPIs for comparison between fully sensible and hybrid SHTES

### 3.2.2 Financial and environmental considerations.

Figure 28 compares the total capital investment (CAPEX) and annual operational (OPEX) costs for the RBS concept in both system variations.

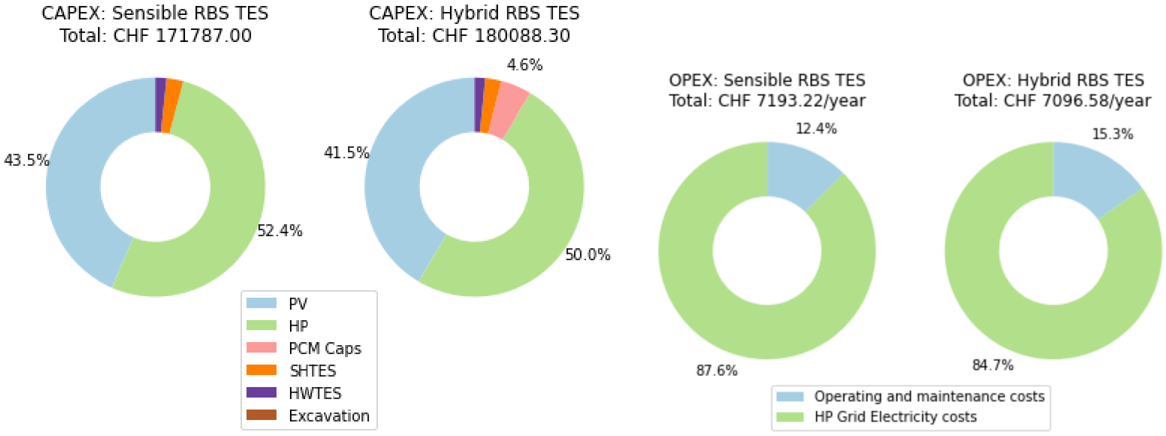

Figure 28 CAPEX and OPEX comparison between sensible and hybrid SHTES RBS.

In the RBS concept, the heat pump and PV system are the primary cost drivers, accounting for over 90% of the total investment. The storage system costs are minimal due to low specific costs and the lack of container material or excavation expenses. Figure 29 compares the CAPEX for an analogous system using VIT (Vacuum Insulated Tank) and SST (Spherical Storage Tank) concepts.

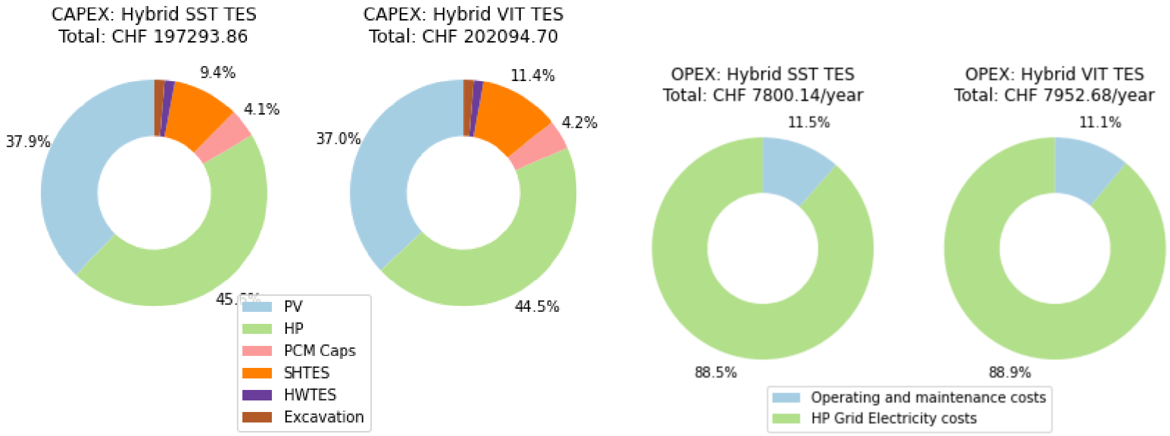

Figure 29 CAPEX and OPEX comparison between sensible and hybrid SHTES using VIT and SST concepts.

Differences in costs and KPIs are due to variations in packing density and volume distribution in spherical and cylindrical storage concepts. Table 13 summarizes the results for the VIT and RBS concepts.

| | VIT SHTES | SST SHTES |
|---|---|---|
| **Self-Sufficiency Thermal [%]** | 84.7 | 84.8 |
| **LCOH [CHF/kWh]** | 0.376 | 0.363 |
| **GWP [CHF/kWh]** | 1.37E-02 | 1.22E-02 |
| **Self-Sufficiency Electric [%]** | 40.5 | 40.4 |
| **PV Self-Consumption [%]** | 44.0 | 44.3 |
| **Comfort level [%]** | 99.1 | 98.9 |

Table 13 Summary of KPIs for example system with VIT and RBS concepts.

Figure 30 shows the GWP contributions from different system components for both RBS variations and the hybrid VIT and SST concepts. The PV system is the largest GWP contributor, accounting for up to 63.7%.

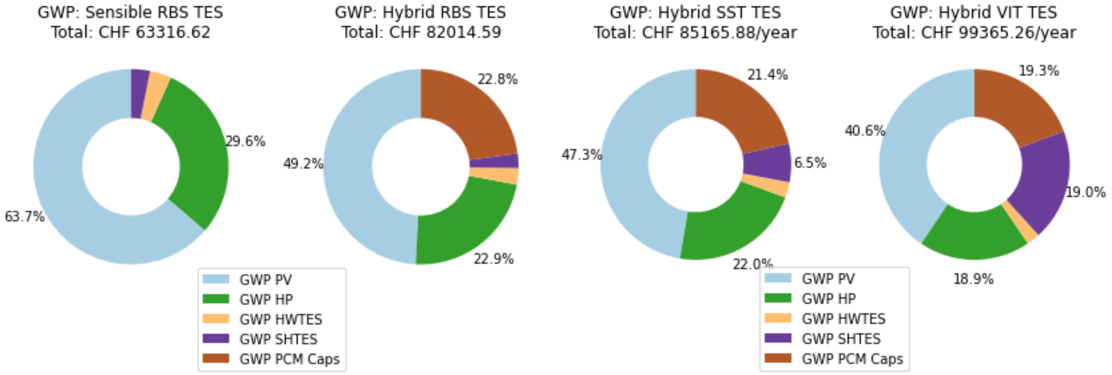

Figure 30 Comparison of GPW for all variations of the example system.

For the RBS concept, the storage GWP is negligible, while for the VIT concept, the storage alone accounts for about 27% of the total due to substantial steel usage and manufacturing processes. PCM capsules hold the second-largest share among hybrid systems, with up to 22.8% for the RBS concept with high packing density.

## 3.3 Optimization

### 3.3.1 Optimization Results

Optimization runs were performed for each storage concept, covering a range of weights ($w_{ss}$ =0.1 to $w_{ss}$=0.9). Figure 31 presents a 3D plot of KPIs: LCOH, $SS_{th}$, and GWP.

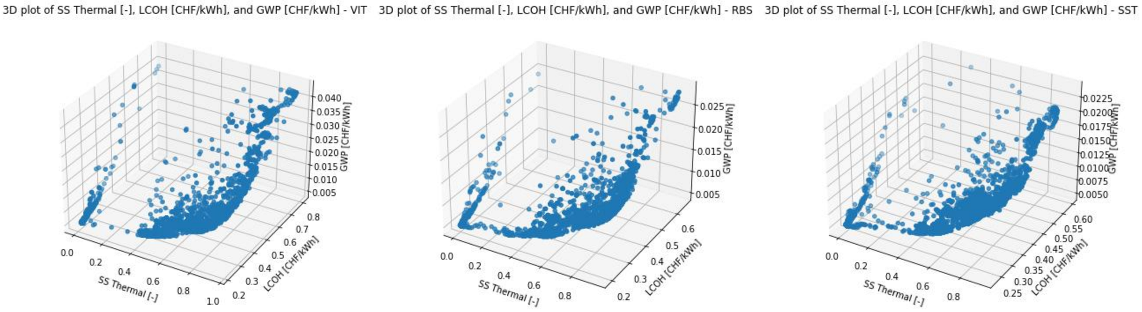

Figure 31 3D representation of optimization outputs as the three KPIs for the optimization objective.

The results were simplified into 2D plots with GWP represented as a heatmap revealing trends where systems nearing 100% self-sufficiency exhibit exponential increases in costs and GWP. Figure 32 presents the datasets obtained for all three concepts. Along with the optimization outputs, the base case is shown with a star to make it easily comparable with the current set of solutions.

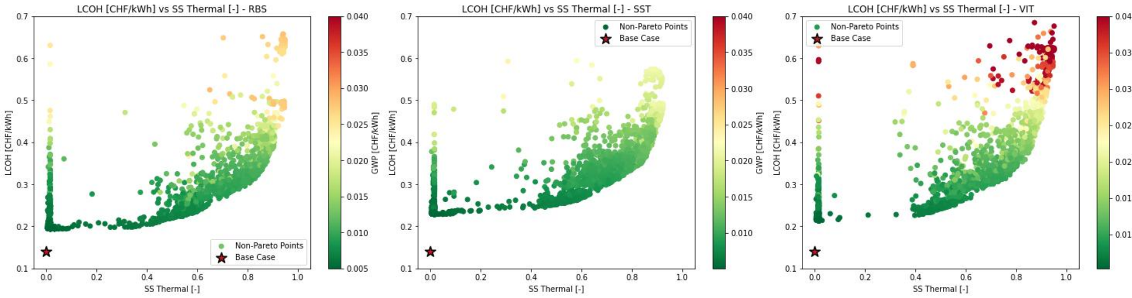

Figure 32 Costs vs thermal self-sufficiency for the three storage concepts.

Overall, none of the solutions at any level of self-sufficiency were cheaper than the oil boiler base case, though most exhibited much lower GWP. It is important to note that these results do not consider subsidies for component purchases or feed-in tariffs from excess electricity delivered to the grid, under the assumption that the system should be viable without such support. At low levels of self-sufficiency (around 50%), costs and GWP remain manageable. However, as self-sufficiency targets approach 80-100%, the required component sizes, costs, and GWP increase exponentially.

#### 3.3.1.1 Pareto fronts: Optimal solution sets

Pareto optimal solution set analysis was performed using the full optimization dataset to identify the optimal solutions across the entire range and understand the relationship between costs, GWP, and self-sufficiency for the three storage unit types. Figure 33 shows the identified Pareto front solutions for each concept.

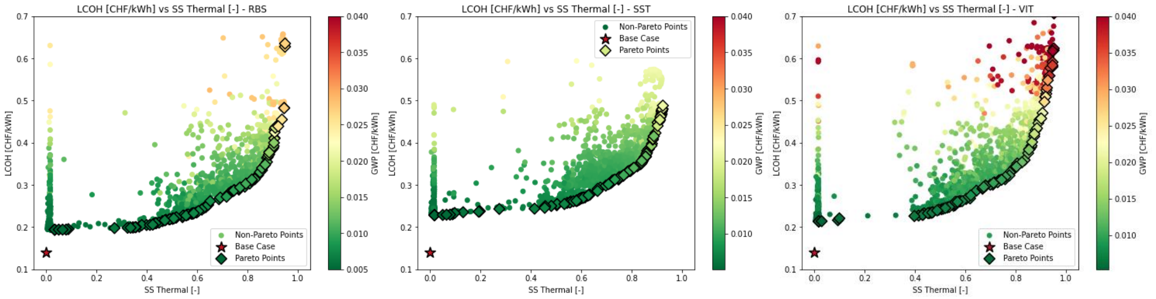

Figure 33 Identified pareto fronts on each concept.

Further analysis of the Pareto front datasets, illustrated in Figure 34, reveals the main points from the LCOH vs SS<sub>th</sub> perspective. Each Pareto front corresponds to an optimal solution dataset for each system.

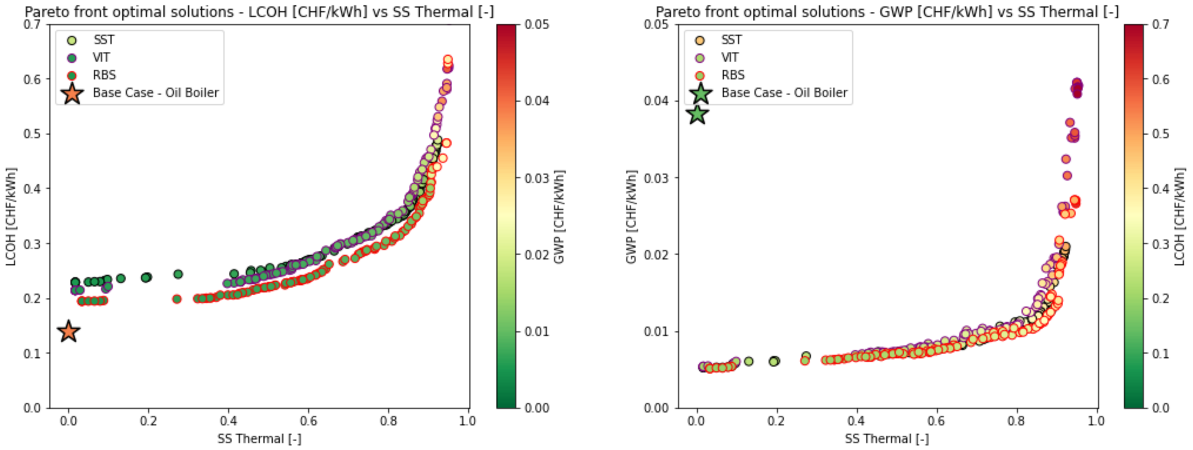

Figure 34 Comparison of pareto front optimal solution subsets for the three storage concepts.

Across the optimal sets for the different storage concepts, the RBS concept marginally outperforms the other two in terms of both LCOH and GWP for self-sufficiency levels below 85%. This advantage is attributed to the lower material and installation costs from repurposing basement space, which requires investment primarily in advanced insulation and waterproofing materials.

Additionally, at self-sufficiency levels around 50% and below, costs remain nearly constant, indicating that minimal investments can cover a significant portion of the demand. However, for higher targets, the necessary over-dimensioning heavily affects both LCOH and GWP. If subsidies and PV sell-back to the grid were considered, the system's LCOH could become competitive with currently used oil boilers, significantly reducing GWP. Nonetheless, a truly scalable solution should be independent of subsidies and feed-in tariffs, which have the potential to fluctuate.

#### 3.3.1.2 Statistical analysis of results

The statistical analysis employed a two-pronged approach: Analysis of Variance (ANOVA) and correlation analysis. ANOVA was utilized to discern the impact of input parameters on the designated KPIs, determining their statistical significance and highlighting pivotal variables in system performance and optimization. Correlation analysis further scrutinized the linear interdependencies among variables, providing a quantified measure of association between each input variable and KPI, and among the KPIs themselves.

**ANOVA for full datasets**

To understand the macro scale of the optimization data obtained, an analysis of variance (ANOVA) was applied to the complete optimization datasets. The analysis allows the identification of statistical significance of different variables on the KPIs. To minimize collinearity some variables such as TES dimensions were bundled into a single volume parameter.

Table 14 summarizes the p-values obtained for the VIT concept, revealing that parameters such as PV peak power and HP peak power are significant. Based on these p-values, it is evident that all the chosen parameters are statistically significant in their relationship with at least one of the proposed KPIs. Specifically, PV peak power, HP peak power, and SHTES volume have the highest statistical significance, making them key drivers of performance, cost, and GWP.

| | p-SS Thermal [-] | p-LCOH | p-GWP |
|---|---|---|---|
| **PV Peak Power [kW]** | 0.00E+00 | 2.01E-137 | 1.81E-130 |
| **PV Azimuth [deg]** | 5.06E-75 | 1.26E-06 | 1.88E-02 |
| **PV Tilt [deg]** | 1.14E-13 | 1.16E-01 | 2.70E-01 |
| **HP Peak Power [kW]** | 5.09E-27 | 0.00E+00 | 3.70E-193 |
| **HyTES Volume [m3]** | 2.59E-40 | 0.00E+00 | 0.00E+00 |
| **PCM Capsule Size [m3]** | 5.18E-01 | 1.94E-46 | 1.73E-04 |
| **PCM Rel. Size [-]** | 3.90E-04 | 6.32E-41 | 7.85E-117 |
| **DHW TES Volume [m3]** | 2.47E-08 | 6.69E-01 | 6.57E-01 |
| **PCM Capsule Index [m3]** | 3.21E-01 | 7.07E-01 | 5.29E-01 |
| **PCM material Index [m3]** | 2.70E-15 | 8.26E-04 | 8.09E-07 |

Table 14 Summary of p-values for ANOVA performed on VIT full optimization dataset.

**Correlation analysis for full datasets**

Correlation analysis methodically explored how different variables within the optimization datasets were related, providing a numerical measurement (correlation coefficient) ranging from -1 (perfect negative correlation) to 1 (perfect positive correlation). Spearman correlation analysis was chosen as it allows for measuring relationships between variables that are not necessarily linear and accounts for rank-order correlation.

The full correlation matrix for the VIT concept, shown in Figure 35, indicated a high positive correlation between the three KPIs. Generally, a larger system tends to lead to higher GWP and SS. Additionally, there was a notable correlation between some parameters, such as higher PV peak power often requiring a larger heat pump and storage, as reflected by the correlation coefficients.

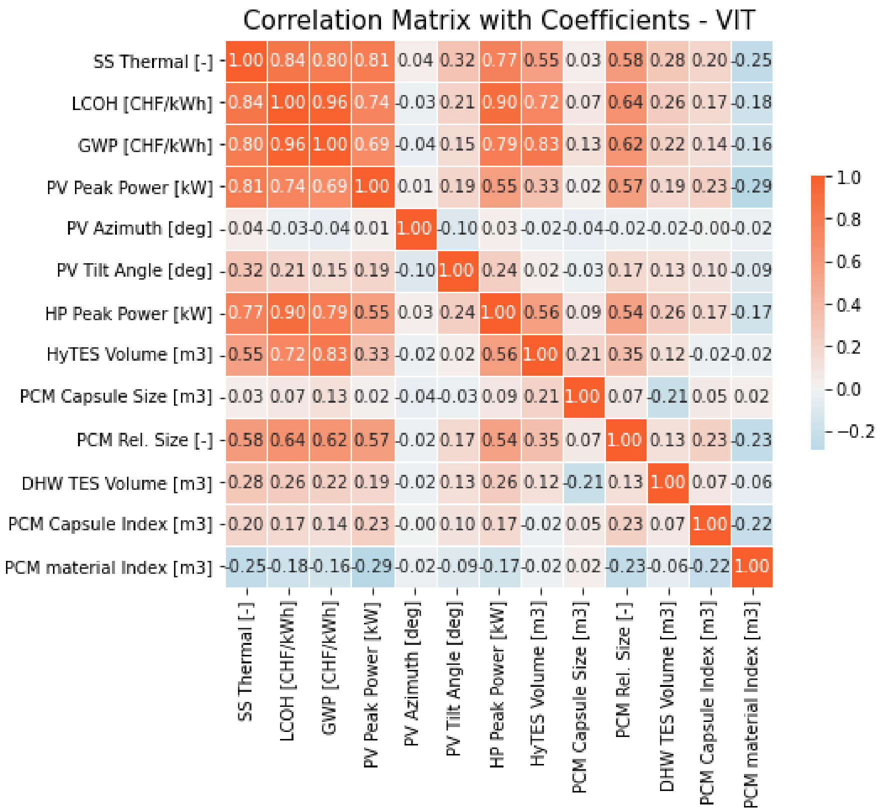

| | SS Thermal [-] | LCOH [CHF/kWh] | GWP [CHF/kWh] | PV Peak Power [kW] | PV Azimuth [deg] | PV Tilt Angle [deg] | HP Peak Power [kW] | HyTES Volume [m3] | PCM Capsule Size [m3] | PCM Rel. Size [-] | DHW TES Volume [m3] | PCM Capsule Index [m3] | PCM material Index [m3] |
|---|---|---|---|---|---|---|---|---|---|---|---|---|---|
| SS Thermal [-] | 1.00 | 0.84 | 0.80 | 0.81 | 0.04 | 0.32 | 0.77 | 0.55 | 0.03 | 0.58 | 0.28 | 0.20 | -0.25 |
| LCOH [CHF/kWh] | 0.84 | 1.00 | 0.96 | 0.74 | -0.03 | 0.21 | 0.90 | 0.72 | 0.07 | 0.64 | 0.26 | 0.17 | -0.18 |
| GWP [CHF/kWh] | 0.80 | 0.96 | 1.00 | 0.69 | -0.04 | 0.15 | 0.79 | 0.83 | 0.13 | 0.62 | 0.22 | 0.14 | -0.16 |
| PV Peak Power [kW] | 0.81 | 0.74 | 0.69 | 1.00 | 0.01 | 0.19 | 0.55 | 0.33 | 0.02 | 0.57 | 0.19 | 0.23 | -0.29 |
| PV Azimuth [deg] | 0.04 | -0.03 | -0.04 | 0.01 | 1.00 | -0.10 | 0.03 | -0.02 | -0.04 | -0.02 | -0.02 | -0.00 | -0.02 |
| PV Tilt Angle [deg] | 0.32 | 0.21 | 0.15 | 0.19 | -0.10 | 1.00 | 0.24 | 0.02 | -0.03 | 0.17 | 0.13 | 0.10 | -0.09 |
| HP Peak Power [kW] | 0.77 | 0.90 | 0.79 | 0.55 | 0.03 | 0.24 | 1.00 | 0.56 | 0.09 | 0.54 | 0.26 | 0.17 | -0.17 |
| HyTES Volume [m3] | 0.55 | 0.72 | 0.83 | 0.33 | -0.02 | 0.02 | 0.56 | 1.00 | 0.21 | 0.35 | 0.12 | -0.02 | -0.02 |
| PCM Capsule Size [m3] | 0.03 | 0.07 | 0.13 | 0.02 | -0.04 | -0.03 | 0.09 | 0.21 | 1.00 | 0.07 | -0.21 | 0.05 | 0.02 |
| PCM Rel. Size [-] | 0.58 | 0.64 | 0.62 | 0.57 | -0.02 | 0.17 | 0.54 | 0.35 | 0.07 | 1.00 | 0.13 | 0.23 | -0.23 |
| DHW TES Volume [m3] | 0.28 | 0.26 | 0.22 | 0.19 | -0.02 | 0.13 | 0.26 | 0.12 | -0.21 | 0.13 | 1.00 | 0.07 | -0.06 |
| PCM Capsule Index [m3] | 0.20 | 0.17 | 0.14 | 0.23 | -0.00 | 0.10 | 0.17 | -0.02 | 0.05 | 0.23 | 0.07 | 1.00 | -0.22 |
| PCM material Index [m3] | -0.25 | -0.18 | -0.16 | -0.29 | -0.02 | -0.09 | -0.17 | -0.02 | 0.02 | -0.23 | -0.06 | -0.22 | 1.00 |

Figure 35 Full correlation matrix for VIT full data set from optimization.

A summary of the correlation analysis with the input variables and KPIs is presented in Figure 36. The main drivers identified include the PV system, heat pump, and SHTES size and PCM configuration. The prohibitive price of using a VIT concept with high shares of PCM at the lowest phase change temperature (40℃) requires volume minimization of the expensive container. To balance the price, the capsule size is proportionally increased to optimize performance, sacrificing power for capacity.

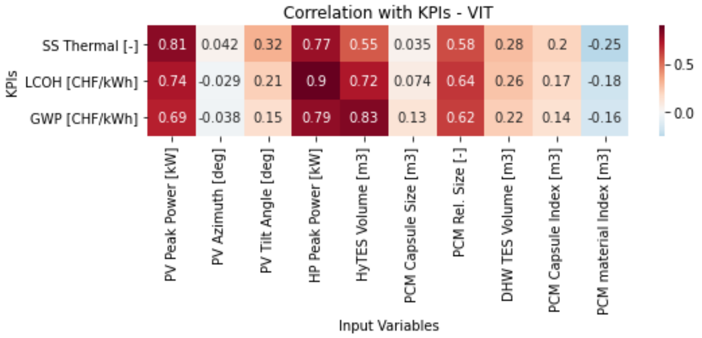

| | PV Peak Power [kW] | PV Azimuth [deg] | PV Tilt Angle [deg] | HP Peak Power [kW] | HyTES Volume [m3] | PCM Capsule Size [m3] | PCM Rel. Size [-] | DHW TES Volume [m3] | PCM Capsule Index [m3] | PCM material Index [m3] |
|---|---|---|---|---|---|---|---|---|---|---|
| SS Thermal [-] | 0.81 | 0.042 | 0.32 | 0.77 | 0.55 | 0.035 | 0.58 | 0.28 | 0.2 | -0.25 |
| LCOH [CHF/kWh] | 0.74 | -0.029 | 0.21 | 0.9 | 0.72 | 0.074 | 0.64 | 0.26 | 0.17 | -0.18 |
| GWP [CHF/kWh] | 0.69 | -0.038 | 0.15 | 0.79 | 0.83 | 0.13 | 0.62 | 0.22 | 0.14 | -0.16 |

Figure 36 Correlation matrix of KPIs vs optimization variables using the full dataset for VIT concept.

### Correlation analysis for pareto optimal solutions dataset

When applying the same correlation analysis to the restricted Pareto front optimal solution datasets, the results closely mirrored those of the full datasets. Figure 37 presents the summarized correlation matrix for the KPIs vs influencing factors.

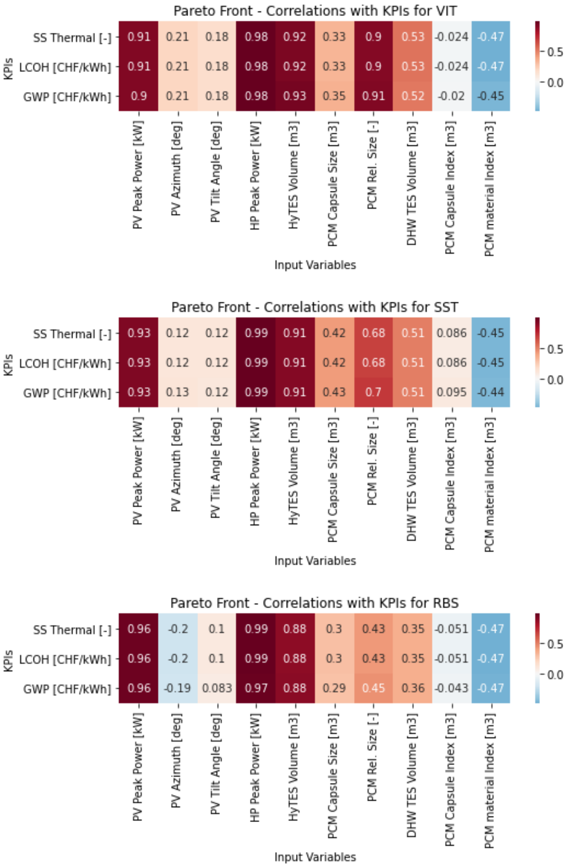

Pareto Front - Correlations with KPIs for VIT

| KPIs | PV Peak Power [kW] | PV Azimuth [deg] | PV Tilt Angle [deg] | HP Peak Power [kW] | HyTES Volume [m3] | PCM Capsule Size [m3] | PCM Rel. Size [-] | DHW TES Volume [m3] | PCM Capsule Index [m3] | PCM material Index [m3] |
|---|---|---|---|---|---|---|---|---|---|---|
| SS Thermal [-] | 0.91 | 0.21 | 0.18 | 0.98 | 0.92 | 0.33 | 0.9 | 0.53 | -0.024 | -0.47 |
| LCOH [CHF/kWh] | 0.91 | 0.21 | 0.18 | 0.98 | 0.92 | 0.33 | 0.9 | 0.53 | -0.024 | -0.47 |
| GWP [CHF/kWh] | 0.9 | 0.21 | 0.18 | 0.98 | 0.93 | 0.35 | 0.91 | 0.52 | -0.02 | -0.45 |

Pareto Front - Correlations with KPIs for SST

| KPIs | PV Peak Power [kW] | PV Azimuth [deg] | PV Tilt Angle [deg] | HP Peak Power [kW] | HyTES Volume [m3] | PCM Capsule Size [m3] | PCM Rel. Size [-] | DHW TES Volume [m3] | PCM Capsule Index [m3] | PCM material Index [m3] |
|---|---|---|---|---|---|---|---|---|---|---|
| SS Thermal [-] | 0.93 | 0.12 | 0.12 | 0.99 | 0.91 | 0.42 | 0.68 | 0.51 | 0.086 | -0.45 |
| LCOH [CHF/kWh] | 0.93 | 0.12 | 0.12 | 0.99 | 0.91 | 0.42 | 0.68 | 0.51 | 0.086 | -0.45 |
| GWP [CHF/kWh] | 0.93 | 0.13 | 0.12 | 0.99 | 0.91 | 0.43 | 0.7 | 0.51 | 0.095 | -0.44 |

Pareto Front - Correlations with KPIs for RBS

| KPIs | PV Peak Power [kW] | PV Azimuth [deg] | PV Tilt Angle [deg] | HP Peak Power [kW] | HyTES Volume [m3] | PCM Capsule Size [m3] | PCM Rel. Size [-] | DHW TES Volume [m3] | PCM Capsule Index [m3] | PCM material Index [m3] |
|---|---|---|---|---|---|---|---|---|---|---|
| SS Thermal [-] | 0.96 | -0.2 | 0.1 | 0.99 | 0.88 | 0.3 | 0.43 | 0.35 | -0.051 | -0.47 |
| LCOH [CHF/kWh] | 0.96 | -0.2 | 0.1 | 0.99 | 0.88 | 0.3 | 0.43 | 0.35 | -0.051 | -0.47 |
| GWP [CHF/kWh] | 0.96 | -0.19 | 0.083 | 0.97 | 0.88 | 0.29 | 0.45 | 0.36 | -0.043 | -0.47 |

Figure 37 Summary of correlation analysis on pareto front data sets for the three storage concepts.

The results show a strong correlation between the three KPIs, with similar correlation coefficients. The primary contributors were the PV system, HP peak power, SHTES and DHW storage volumes, and PCM configurations.

For all three concepts, the main driver was the HP peak power, followed by PV peak power and SHTES size. As specific costs increased (RBS, SST, and VIT), so did the correlation index of the PCM relative size, up to 0.9 for the most expensive VIT concept. This trend also applied to the DHW tank, as minimizing SHTES volume became a priority to keep LCOH and GWP down. For RBS, reduced manufacturing and installation costs made storage size a key driver only for thermal self-sufficiency.

Larger PCM capsules, which have lower specific heat transfer surfaces, limit the unit's power output, reducing the amount of usable hot water during high demand. However, smaller sizes significantly drove LCOH and GWP up due to higher manufacturing costs and the cost of encapsulation. Thus, the PCM capsule size remained a compromise between performance and cost. Similarly, a lower phase change temperature for PCM was beneficial across all cases, as it allowed enough temperature difference for both charging and discharging processes, leading to more effective utilization of PCM's added capacity.

The DHW tank had a clear influence on all KPIs, as it was crucial for achieving high levels of self-sufficiency by providing additional capacity when SHTES was full, and PV power was still available for the HP. Across all cases, the HWTES volume exceeded daily requirements and would only charge the necessary buffer zone for a day's worth of service with grid power if needed. This, in turn, minimized SHTES volume as the system strived to provide both services, increasing the rate of SHTES usage with the large amount of PV power available and allowing cheaper HWTES to be used for more than daily storage.

### Optimal configuration samples for all three concepts

Table 15 provides a summary of KPIs and inputs for selected points for each storage concept at increasing thermal self-sufficiency levels, ranging from 70% to 95.6%. Three representative points are displayed for each concept, with the closest point to each target chosen for practical purposes. Other configurations can generate similar KPIs due to the high nonlinearity of the relationships between parameters and KPIs.

| **SUMMARY** | **SST** | | | **VIT** | | | **RBS** | | |
|---|---|---|---|---|---|---|---|---|---|
| **SS Thermal [%]** | 70.8 | 85.0 | 92.4 | 69.9 | 85.3 | 95.6 | 68.6 | 84.9 | 94.9 |
| **LCOH [CHF/kWh]** | 0.30 | 0.36 | 0.49 | 0.30 | 0.38 | 0.79 | 0.27 | 0.33 | 0.63 |
| **GWP [CHF/kWh]** | 0.009 | 0.012 | 0.021 | 0.010 | 0.013 | 0.042 | 0.008 | 0.010 | 0.027 |
| **SS Electric [%]** | 37.9 | 40.3 | 41.0 | 39.1 | 40.5 | 41.1 | 38.5 | 40.6 | 41.3 |
| **PV Self-Cons. [%]** | 45.7 | 45.3 | 47.8 | 38.6 | 44.3 | 48.3 | 43.4 | 44.8 | 49.6 |
| **Comfort level [%]** | 98.4 | 98.9 | 99.5 | 97.9 | 99.2 | 99.6 | 98.1 | 99.2 | 99.6 |
| **PV [kWp]** | **30.4** | **35.3** | **36.1** | **36.1** | **36.1** | **36.1** | **31.5** | **36.1** | **36.1** |
| **PV [m2]** | 146.0 | 169.7 | 173.3 | 151.4 | 173.3 | 173.3 | 173.3 | 173.3 | 173.3 |
| **PV Tilt [deg]** | 45 | 45 | 45 | 45 | 45 | 45 | 45 | 45 | 45 |
| **PV Azimuth [deg]** | 180 | 180 | 180 | 190 | 180 | 180 | 190 | 190 | 190 |
| **HP Peak Power [kWe]** | **8.5** | **15.5** | **24.5** | **7.5** | **16.5** | **24.0** | **7.5** | **15.5** | **23.0** |
| **SHTES Vol. [m3]** | **4.06** | **7.70** | **33.51** | **2.26** | **7.74** | **70.00** | **3.95** | **17.61** | **65.97** |
| **SHTES Height [m]** | 0.00 | 0.00 | 0.00 | 2.00 | 2.00 | 3.95 | 3.95 | 2.73 | 3.74 |
| **SHTES Dimension [m]** | 1.98 | 2.45 | 4.00 | 1.20 | 2.22 | 4.75 | 1.00 | 2.54 | 4.20 |
| **HWTES Vol. [m3]** | **3.07** | **2.45** | **3.07** | **2.38** | **2.61** | **3.07** | **2.18** | **2.27** | **3.07** |
| **HWTES Height [m]** | 2.50 | 2.00 | 2.50 | 2.50 | 2.23 | 2.50 | 1.78 | 1.97 | 2.50 |
| **HWTES Dimension [m]** | 1.25 | 1.25 | 1.25 | 1.10 | 1.22 | 1.25 | 1.25 | 1.21 | 1.25 |
| **PCM Rel. Height [%]** | **10** | **80** | **80** | **45** | **90** | **90** | **10** | **10** | **90** |
| **PCM Rel. Vol [%]** | 1.5 | 50.1 | 51.5 | 26.1 | 52.1 | 44.2 | **5.1** | **5.7** | **46.1** |
| **PCM Capsule Size [L]** | 1.10 | 1.70 | 5.00 | 2.55 | 2.25 | 0.10 | 0.10 | 4.20 | 0.10 |
| **PCM Capsule Index [-]** | 4 | 4 | 4 | 4 | 4 | 4 | 1 | 2 | 2 |
| **PCM material Index [-]** | 1 | 1 | 1 | 1 | 1 | 1 | 1 | 1 | 1 |

Table 15 Summary of example optimal configurations for the three storage concepts at self-sufficiency objectives between 70 and 100%

Overall, for self-sufficiencies around 85% and below, all parameters remain within the optimization range. For cases closest to 100% self-sufficiency, systems partially reach the limits of the domain, such as maximizing PV amounts for higher cases. The specific costs of storage concepts are also highlighted. For the RBS and SST concepts, the maximum share of PCM is only used for cases closest to 100%

self-sufficiency. For the VIT concept, as PCM costs become more competitive with the large tank investment, the share is 45% even at lower self-sufficiency levels and maximized for higher levels. In these cases, as PCM becomes dominant, capsule size is minimized to ensure optimal performance.

Table 16 summarizes the investment costs for all nine example points on the Pareto front. In all cases, the required heat pump (HP) and photovoltaic (PV) system were the main cost drivers. For higher levels of self-sufficiency, the HP size was increased to match the increasing amounts of PV.

| **INVESTMENTS** | **SST** | | | **VIT** | | | **RBS** | | |
|---|---|---|---|---|---|---|---|---|---|
| **PV [kCHF]** | 66.7 | 73.7 | 74.8 | 74.8 | 74.8 | 74.8 | 68.4 | 74.8 | 74.8 |
| **HP [kCHF]** | 59.6 | 92.4 | 134.3 | 55.0 | 97.0 | 132.0 | 55.0 | 92.3 | 127.3 |
| **PCM Caps [kCHF]** | 0.1 | 6.9 | 27.8 | 1.0 | 6.9 | 162.2 | 1.0 | 1.6 | 150.7 |
| **SHTES [kCHF]** | 17.7 | 18.3 | 31.2 | 11.2 | 20.8 | 63.2 | 2.8 | 6.3 | 15.3 |
| **HWTES [kCHF]** | 5.9 | 4.2 | 5.9 | 5.3 | 4.8 | 5.9 | 3.5 | 4.0 | 5.9 |
| **Excavation [kCHF]** | 2.6 | 2.9 | 5.1 | 2.4 | 2.9 | 8.2 | 0.0 | 0.0 | 0.0 |
| **Total (CAPEX) [kCHF]** | 152.7 | 198.3 | 279.1 | 149.7 | 207.2 | 446.2 | 130.6 | 179.0 | 374.1 |
| **Op. costs (OPEX) [kCHF/year]** | 5.3 | 6.9 | 9.8 | 5.2 | 7.3 | 15.6 | 4.6 | 6.3 | 13.1 |
| **HP Grid costs [kCHF/year]** | 1.5 | 0.9 | 0.5 | 1.5 | 0.9 | 0.4 | 1.6 | 0.8 | 0.4 |

Table 16 Summary of investment costs for example optimal configurations for the three storage concepts at self-sufficiency objectives between 70 and 100%

The SHTES contribution was almost negligible in RBS systems. For SST, costs remain similar throughout due to a reduced diameter range set by the manufacturer. For VIT, with higher specific prices and GWP, solutions converge towards smaller storage volumes (2.26 m³ to 70 m³) fully packed with PCM capsules. This configuration is beneficial in both LCOH and GWP.

Table 17 shows the GWP contributions for the example optimum points. The PV system is the primary GWP driver, accounting for 60% to 83% of the total system GWP in all cases. Other significant contributions come from PCM and storage tank volumes, especially for the VIT concept.

| **GWP** | **SST** | | | **VIT** | | | **RBS** | | |
|---|---|---|---|---|---|---|---|---|---|
| **PV [tCO2eq]** | 34.0 | 39.5 | 40.3 | 40.3 | 40.3 | 40.3 | 35.2 | 40.3 | 40.3 |
| **HP [tCO2eq]** | 7.6 | 20.0 | 46.9 | 6.5 | 22.3 | 45.1 | 6.5 | 19.9 | 41.6 |
| **SHTES [tCO2eq]** | 3.4 | 5.0 | 12.3 | 5.4 | 15.7 | 132.7 | 1.3 | 3.0 | 7.1 |
| **PCM [tCO2eq]** | 0.3 | 15.2 | 66.2 | 2.3 | 15.8 | 142.6 | 0.9 | 3.8 | 133.3 |
| **HWTES [tCO2eq]** | 3.6 | 2.9 | 3.6 | 2.8 | 3.1 | 3.6 | 2.6 | 2.7 | 3.6 |
| **Grid [tCO2eq/year]** | 1.6 | 1.4 | 1.2 | 1.6 | 1.3 | 1.2 | 1.6 | 1.3 | 1.2 |

Table 17 Summary of GWP for example optimal configurations for the three storage concepts at self-sufficiency objectives between 70 and 100%

### 3.3.2 Study on Best Case Scenarios (PV and PCM)

This section explores the influence of PV and PCM costs and GWP projections through a series of isolated and combined best-case scenarios. The analysis is conducted in three steps: examining the impact of PV cost functions, evaluating PCM price and GWP projections, and assessing the combined best-case scenario.

#### Influence of PV cost function

To understand the impact of varying PV costs, the study was reproduced using cost functions from 2019 and the most recent 2023 versions, adjusted for current global economic conditions. The Pareto front data for these scenarios, summarized in Figure 38, indicate a significant increase in PV costs between 2019 and 2023, leading to an overall rise in LCOH for all system configurations.

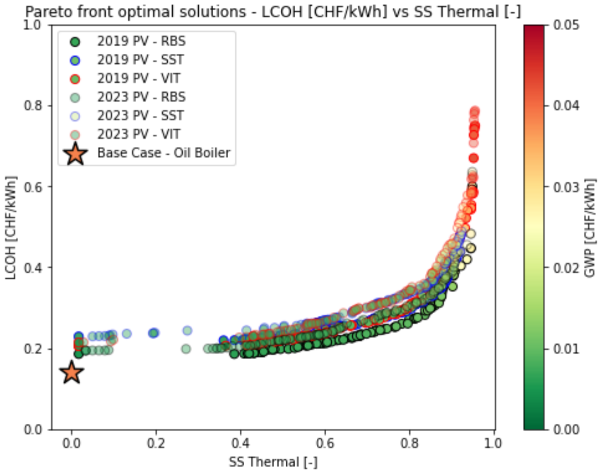

Figure 38 Comparison of PV cost functions for 2023 and 2019 for all 3 storage concepts.

Despite the cost increase, the essential role of PV in covering a sizable portion of the energy demand remains unchanged, as the required storage volumes remain constant across scenarios. The cost increase is primarily attributed to higher PV installation expenses. The results underscore the need to re-evaluate economic viability considering elevated PV costs, particularly in scenarios without financial incentives or subsidies. The robustness of PV installations in achieving energy self-sufficiency highlights their critical importance, even in less favorable economic conditions.

#### Influence of PCM price and GWP.

The focus shifts to PCM price and GWP projections, which show more variability in system configurations compared to PV costs. In a best-case scenario, it is estimated by COWA TS that the PCM price will decrease by 50% of the current price. Additionally, expected improvements in the production process are projected to reduce the total GWP by 70% per capsule.

The analysis demonstrates how reducing the relative price and GWP contribution of PCM capsules affects the system's design and performance, as shown in Figure 39.

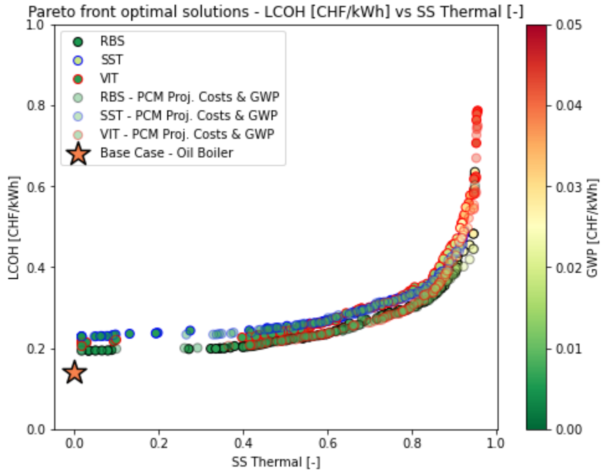

Figure 39 Comparison of best-case scenario costs and GWP projection for the selected PCMs with the current state.

By decreasing the relative price and GWP contribution of PCM capsules, their usage is incentivized for higher $SS_{th}$ values. Comparing the current prices and GWP estimations versus the projected best-case scenario for PCM, the configurations obtained differ significantly, particularly for the RBS concept. The optimizer increases the share of PCM, especially in the 80-90% $SS_{th}$ range, while keeping the overall volume as low as possible. This strategy leverages PCM's thermal storage benefits without incurring excessive costs.

The RBS concept, used as the base case due to its lower cost, highlights the increased PCM usage in this scenario. This configuration helps understand the potential economic and environmental benefits of lower PCM costs and GWP contributions.

Figure 40 shows the SHTES volume versus $SS_{th}$ for both current and best-case PCM scenarios, demonstrating the impact of PCM price and GWP projections on storage requirements. It also presents the PCM volume within SHTES versus $SS_{th}$, illustrating variations in PCM usage based on cost and GWP projections.

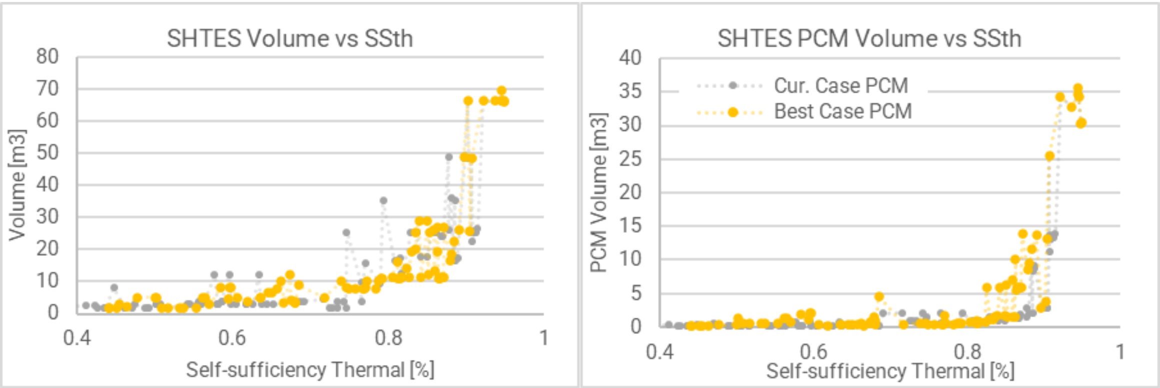

Figure 40 Left: Seasonal hybrid storage volume on the pareto front for increasing levels of self-sufficiency. Right: Volume of PCM on the pareto front for increasing levels of self-sufficiency for RBS concept.

#### **Influence of the combined Best-Case Scenario**

The combined best-case scenario integrates both PV and PCM cost reductions and GWP improvements. The resulting configurations reflect the compounded benefits of the individual optimizations. The overall results are shown in Figure 41, present the most significant improvements in LCOH and GWP. By integrating lower PV costs and improved PCM performance, the system achieves higher $SS_{th}$ values with lower overall costs and environmental impact.

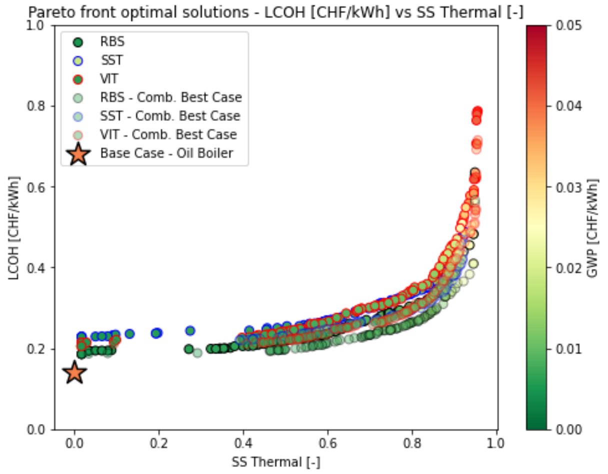

Figure 41 Comparison of the pareto front data sets with the current state and the combined best-case scenario for PV and PCM.

This scenario underscores the potential for future technological and economic advancements to enhance the feasibility and sustainability of hybrid thermal energy storage systems.

Figure 42 illustrates the SHTES volume versus $SS_{th}$ for the combined best-case scenario, and the PCM volume within SHTES versus $SS_{th}$ for various scenarios, highlighting the impact of the combined best-case projections.

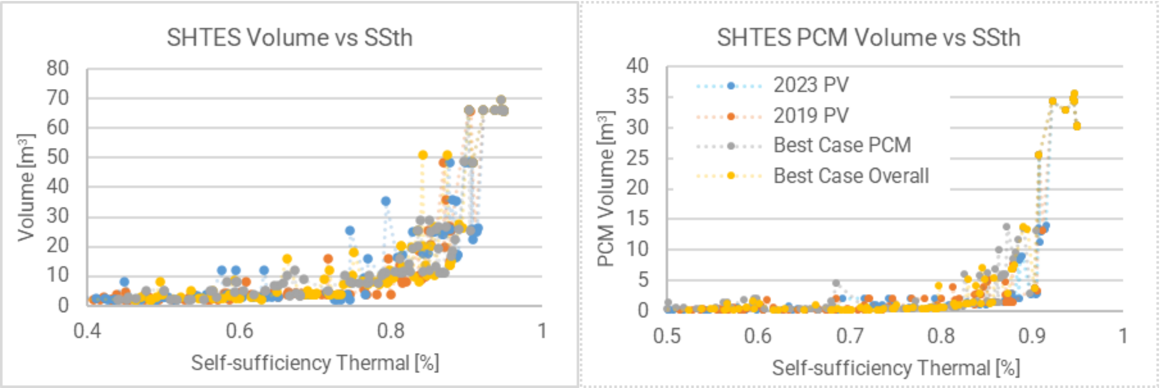

Figure 42 Left: Seasonal hybrid storage volume on the pareto front for increasing levels of self-sufficiency. Right: Volume of on the pareto front for increasing levels of self-sufficiency for RBS concept.

### 3.3.3 Influence of PV maximum roof coverage ratio

This section examines the influence of different PV maximum roof surface coverage ratios on system performance, focusing on PV and HP as primary drivers and their asymptotic behavior up to a certain $SS_{th}$ level. The analysis highlights the critical role of storage capacity as the $SS_{th}$ limit is approached.

Even though the maximum surface limit of 66% of the total roof surface [57] was used in all previous simulations, several scenarios with varying PV coverage (44%, 66%, 88%, and 100% of the total roof surface of 264 m²) were analyzed to understand their impact on system performance, costs, and GWP. The results, summarized in Figure 43, show that even with 44% PV coverage, a significant $SS_{th}$ of 70% can be achieved with relatively low storage volumes (2.5 to 6 m³). This demonstrates that effective use of PV and HP can substantially reduce the need for large storage capacities, especially for lower $SS_{th}$ targets.

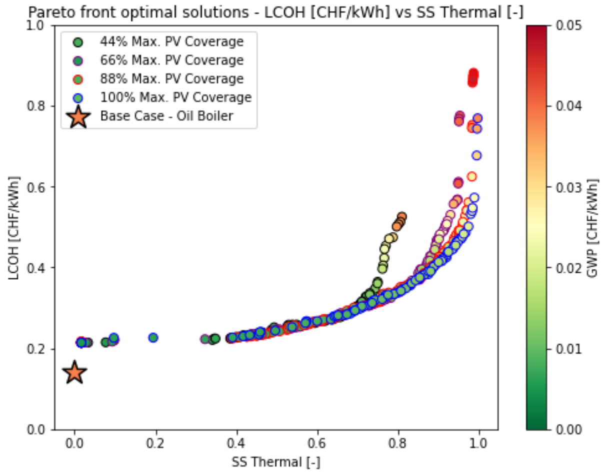

Figure 43 Pareto front datasets for various levels of maximum PV coverage ratio.

For $SS_{th}$ levels of 70% and below, storage capacity operates mainly as short to medium-term storage, with PV/HP combination managing most of the load during the day and stored energy bridging the night gap. As $SS_{th}$ increases past 70%, storage volumes become key based on available PV peak power. Self-consumption rates vary significantly with PV coverage; lower PV coverage aligns closely with immediate energy needs, while higher PV coverage decreases self-consumption rates due to excess energy production, reducing storage volume needs to manage peak demands.

Figure 44 illustrates LCOH and GWP trends for different PV coverage ratios, showing that maximizing PV coverage and HP capacity can achieve high self-sufficiency levels with reasonable storage volumes. However, this approach leads to higher initial costs and increased GWP due to larger storage requirements. While achieving high self-sufficiency is possible with optimal PV and HP integration, it involves trade-offs. For example, the self-consumption rate is 63% in the 44% PV coverage scenario compared to 33% in the 100% PV coverage scenario, highlighting the challenge of balancing high self-sufficiency with efficient use of renewable energy.

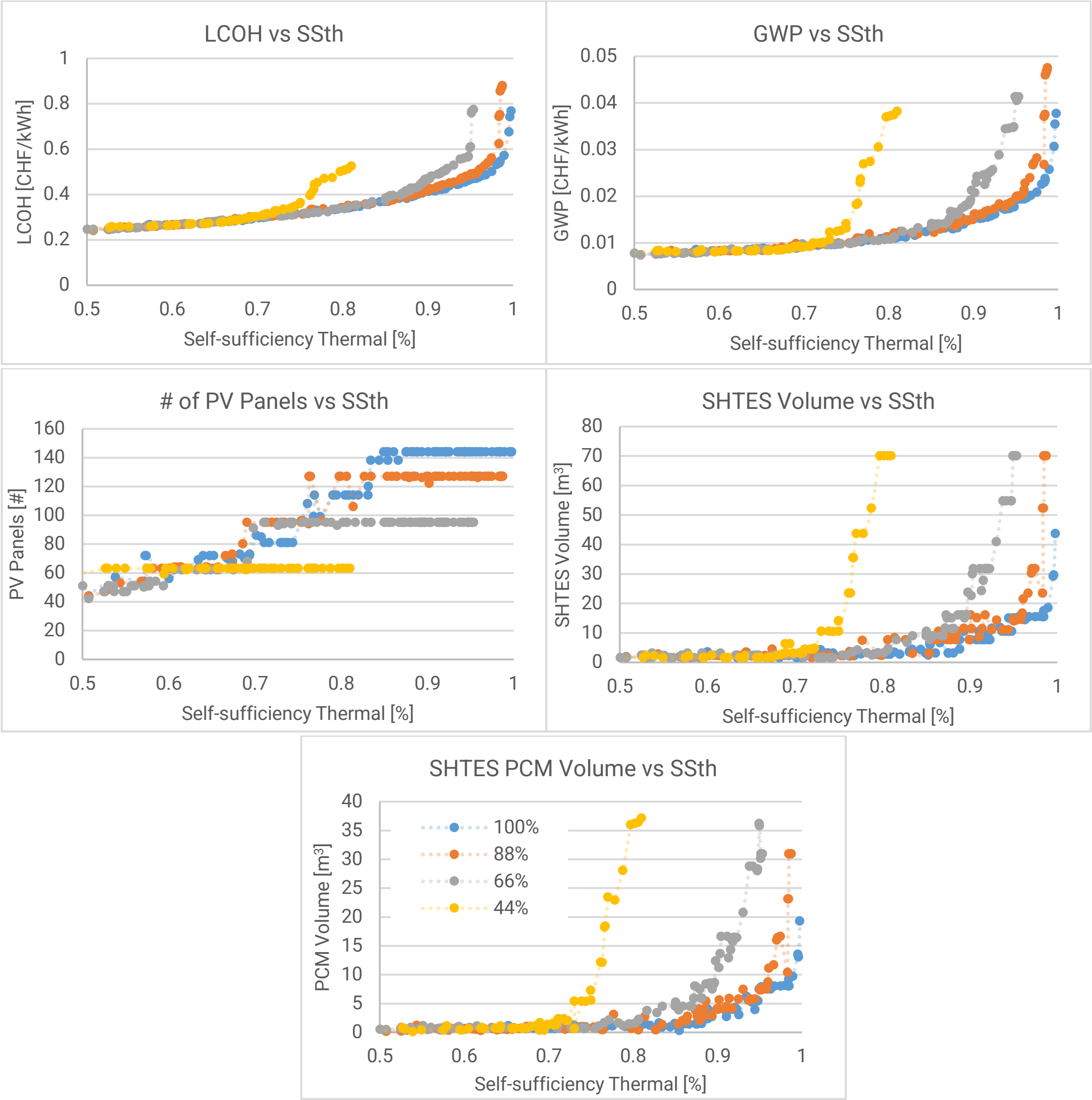

Figure 44 Comparison of several factors for the pareto front datasets produced for VIT at increasing levels of maximum PV coverage ratio.

These findings indicate a threshold beyond which increasing PV coverage yields diminishing returns in terms of economic and environmental benefits. For PV coverage ratios up to 88%, the system can achieve balanced performance with manageable storage volumes and acceptable LCOH and GWP values. To optimize system performance, it is essential to consider the interplay between PV coverage, storage capacity, and self-consumption rates. While higher PV coverage can theoretically achieve near-total self-sufficiency, it requires disproportionately larger storage volumes beyond a certain threshold, which may not be economically or environmentally sustainable.

# 4 Conclusions

This study provides an in-depth analysis of the performance, costs, and environmental impacts of sensible and hybrid sensible-latent seasonal thermal energy storage systems (SHTES). Our findings show that thermal self-sufficiency (SSth) of up to 85% is achievable with an ~8m³ storage system for a multi-family house with 20 inhabitants at reasonable costs. Beyond this capacity, costs and volumes increase exponentially. For SSth below 70%, the system costs are comparable to existing systems but offer a significantly better Global Warming Potential (GWP) than the oil boiler base case. Maximizing PV capacity and selecting an appropriate heat pump (HP) are essential for effective Thermal Energy Storage (TES) in enhancing thermal self-sufficiency.

We introduce a comprehensive model of hybrid sensible-latent thermal energy storage, featuring a fixed bed of randomly arranged PCM macrocapsules. The model considers effects at different scales, from stratification in the sensible part to melting-crystallization of various capsule geometries, and operations from system to component level.

Optimization reveals no single solution that minimizes cost, maximizes self-sufficiency, and reduces GWP simultaneously. Pareto fronts highlight trade-offs, suggesting systems achieving around 70% self-sufficiency are economically feasible with low environmental impacts. Statistical analyses confirm the significant roles of PV peak power, HP capacity, and SHTES volume in influencing key performance indicators (KPIs).

Significant price increases in PV from 2019 to 2023 lead to higher levelized cost of heat (LCOH) for all configurations, yet PV installations remain crucial. Reducing PCM price and GWP encourages higher PCM usage for greater SSth, particularly in the 80-90% range. The best-case scenario with lower PV costs and improved PCM performance shows notable LCOH and GWP improvements, indicating potential future advancements. Overall, the study highlights the necessity of policies to drive renewable heating solutions with respect to still low-cost fossil fuel solutions.

Higher PV coverage ratios impact system performance, with up to 70% SSth achievable with low storage volumes. However, higher SSth with lower PV coverage requires larger storage volumes, increasing costs and GWP. Balancing PV coverage, storage capacity, and self-consumption rates is vital for sustainability. At PV roof surface coverage up to 66%, systems achieve balanced performance with manageable storage volumes and acceptable LCOH and GWP values.

Future research should explore emerging materials and innovative configurations to further reduce costs and GWP. Regulatory and market adjustments could enhance economic viability. Real-world operational simulations would validate and refine optimization models. This research highlights the importance of strategic cost reductions, technological advancements, and supportive policies for efficient, cost-effective, and sustainable energy storage solutions.

# 5 National and international cooperation

As part of the HyTES project, synergies are actively achieved through the creation and coordination of links with national and international business and research partners as well as research projects. Examples of such synergies are used with the following projects and partners:

- PhD project “DESIGN AND OPTIMIZATION OF MACRO-ENCAPSULATION BASED LATENT HEAT ENERGY STORAGE”. Collaboration between EPFL and HSLU. Key findings of the project were applied in HyTES to improve model and system with additional aspects of border effects, capsule shape, and size effects, and how they translate to packed bed characteristics.
- Innosuisse project "GEAS 95" (HSLU and swisspor). The findings of GEAS 95 regarding storage concepts and their costs are used in HyTES. The simulation models from HyTES are used in GEAS 95 to answer various questions - including the influence of the storage temperature and the costs and service life of the insulation material on the heat production costs.
- BFE Project SensOpt (OST-SPF, HSLU and Jenni Energietechnik). The findings of the recently completed SensOpt project are used as a basis in HyTES to further optimize the PV/HP/storage system.
- BFE project 100%SolarLCA (OST-SPF, HSLU, FHNW, Synergie-Plus and Jenni Energietechnik). An LCA of the HyTES system is to be carried out in this project and the measurement data recorded as part of the monitoring in Huttwil are to be used to validate and further develop the HyTES simulation models.
- SWEET PATHFNDR / SWEET EDGE / SWEET DeCarbCH. In these projects, simplified versions of the HyTES simulation models are used to improve the sustainability and flexibility of the Swiss energy system by integrating seasonal thermal energy storage in thermal networks. The results of these projects will in turn quantify the potential of the HyTES storage concept - both at regional and national level.
- SFOEProject IEA Participation IEA ECES Task 35 'Flexible Sector Coupling'. The HyTES concept is included within the sector coupling options.
- SolarBoost InnoBooster project («PCM storage for heat pump systems to boost photovoltaic self-consumption»). The aim of this project was to build a working prototype of the storage system with PCM capsules, which provided the validation data for HyTES. Furthermore, a pilot object was acquired in this project, which can also provide useful data for HyTES in the future. The market launch of the PCM capsules was also included in this project.
- Innovation project SolarStore. In this project, the PCM and encapsulation from the company Cowa Thermal Solutions AG were further developed and finally produced to be tested in the prototype.

# 6 Bibliography

[1] R. J. Hewicker Christian Werner Oliver, Ebert Michael, Dr. Mennel Tim, Dr. Verhaegh Nynke, “Energiespeicher in der Schweiz / Bedarf, Wirtschaftlichkeit und Rahmenbedingungen im Kontext der Energiestrategie 2050,” 2013.

[2] BFE, “Analyse des schweizerischen Energieverbrauchs 2000–2020 nach Verwendungszwecken,” *Bundesamt für Energ.*, no. Oktober, p. 98, 2021.

[3] J. A. Energietechnik, “Solarüberbauung Allmend, Huttwil.” www.jenni.ch (accessed Nov. 18, 2019).

[4] W. Villasmil, M. Troxler, R. Hendry, and J. Worlitschek, “OPTSAIS – Exergetic and Economic Optimization of Seasonal Thermal Energy Storage Systems,” 2019. https://www.aramis.admin.ch/Default?DocumentID=62816&Load=true (accessed Jan. 23, 2021).

[5] R. Stropnik, R. Koželj, E. Zavrl, and U. Stritih, “Improved thermal energy storage for nearly zero energy buildings with PCM integration,” *Sol. Energy*, vol. 190, pp. 420–426, Sep. 2019, doi: 10.1016/j.solener.2019.08.041.

[6] Y. Qin *et al.*, “The effect of phase change material balls on the thermal characteristics in hot water tanks: CFD research,” *Appl. Therm. Eng.*, vol. 178, Sep. 2020, doi: 10.1016/j.applthermaleng.2020.115557.

[7] R. Majumdar and S. K. Saha, “Effect of varying extent of PCM capsule filling on thermal stratification performance of a storage tank,” *Energy*, vol. 178, pp. 1–20, Jul. 2019, doi: 10.1016/j.energy.2019.04.101.

[8] V. Becattini, L. Geissbühler, G. Zanganeh, A. Haselbacher, and A. Steinfeld, “Pilot-scale demonstration of advanced adiabatic compressed air energy storage, Part 2: Tests with combined sensible/latent thermal-energy storage,” *J. Energy Storage*, vol. 17, pp. 140–152, Jun. 2018, doi: 10.1016/j.est.2018.02.003.

[9] W. Villasmil, M. Troxler, R. Hendry, P. Schuetz, and J. Worlitschek, “Control strategies of solar heating systems coupled with seasonal thermal energy storage in self-sufficient buildings,” *J. Energy Storage*, vol. 42, p. 103069, Oct. 2021, doi: 10.1016/j.est.2021.103069.

[10] C. Audet, S. Le Digabel, V. R. Montplaisir, and C. Tribes, “NOMAD version 4: Nonlinear optimization with the MADS algorithm,” Apr. 2021, Accessed: Dec. 16, 2021. [Online]. Available: https://arxiv.org/abs/2104.11627

[11] “Meteonorm Zeitreihen - Meteonorm (de).” https://meteonorm.com/meteonorm-zeitreihen (accessed Sep. 13, 2021).

[12] “SIA 385/1 (2020) Anlagen fur Trinkwarmwasser in Gebäuden - Grundlagen und Anforderungen Referenznummer.” Schweizerischer Ingenieur- und Architektenverein, pp. 1–40, 2020. [Online]. Available: file:///C:/Users/Fabian Barmet/Normen/sia/Disk/385-1_2011_Anlagen für Trinkwarmwasser in Gebäuden_mit Korrigenda_2013.pdf

[13] “SIA 385/1 (2009): Anlagen für Trinkwarmwasser in Gebäuden - Grundlagen und Anforderungen, Norm Ausgabe 2009.” Schweizerischer Ingenieur- und Architektenverein, Zürich, 2011.

[14] “SIA 385/2 (2015): Anlagen für Trinkwarmwasser in Gebäuden - Warmwasserbedarf, Gesamtanforderungen und Auslegung,” Schweizerischer Ingenieur- und Architektenverein, Zürich, 2014.

[15] U. Jordan and K. Vajen, “Influence Of The DHW Load Profile On The Fractional Energy Savings:: A Case Study Of A Solar Combi-System With TRNSYS Simulations,” *Sol. Energy*,

vol. 69, Supple, no. 0, pp. 197–208, 2001, doi: http://dx.doi.org/10.1016/S0038-092X(00)00154-7.

[16] T. Tjaden, B. Joseph, and V. Quaschning, “Repräsentative elektrische Lastprofile für Wohngebäude in Deutschland auf 1-sekündiger Datenbasis,” *HTW Berlin*, no. November, p. 8, 2015.

[17] EnergieSchweiz, “Faktenblatt: Stromverbrauch eines typischen Haushalts,” no. August, pp. 1–3, 2021.

[18] swisspor Management AG and Hochschule Luzern, “Innosuisse Projekt ‘GEAS’ (Projekt-Nr. 27954.1 PFIW-IW).” 2019.

[19] Suntech, “IEC-STP-Ultra-Smini-NO2.02-rev2021,” 2021.

[20] L. Geissbühler, M. Kolman, G. Zanganeh, A. Haselbacher, and A. Steinfeld, “Analysis of industrial-scale high-temperature combined sensible/latent thermal energy storage,” *Appl. Therm. Eng.*, vol. 101, pp. 657–668, 2016, doi: 10.1016/j.applthermaleng.2015.12.031.

[21] P. Schuetz *et al.*, “Fast simulation platform for retrofitting measures in residential heating,” in *Cold Climate HVAC 2018*, D. Johansson, H. Bagge, and Å. Wahlström, Eds., Springer, 2018, pp. 713–723. doi: 10.1007/978-3-030-00662-4_60.

[22] M. Grabo, E. Acar, and E. Y. Kenig, “Modeling and improvement of a packed bed latent heat storage filled with non-spherical encapsulated PCM-Elements,” *Renew. Energy*, vol. 173, pp. 1087–1097, 2021, doi: 10.1016/j.renene.2021.04.022.

[23] S. K. Ashour and M. A. Abdel-hameed, “Approximate skew normal distribution,” *J. Adv. Res.*, vol. 1, no. 4, pp. 341–350, 2010, doi: 10.1016/j.jare.2010.06.004.

[24] J. M. A. Márquez, M. Á. M. Bohórquez, and S. G. Melgar, “Ground thermal diffusivity calculation by direct soil temperature measurement. application to very low enthalpy geothermal energy systems,” *Sensors (Switzerland)*, vol. 16, no. 3, 2016, doi: 10.3390/s16030306.

[25] A. Bellini, S. Bifaretti, V. Iacovone, and C. Cornaro, “Simplified model of a photovoltaic module,” *2009 Appl. Electron. Int. Conf. AE 2009*, no. October, pp. 47–52, 2009.

[26] R. Perez, R. Seals, P. Ineichen, R. Stewart, and D. Menicucci, “A new simplified version of the perez diffuse irradiance model for tilted surfaces,” *Sol. Energy*, vol. 39, no. 3, pp. 221–231, 1987, doi: 10.1016/S0038-092X(87)80031-2.

[27] “NOAA ESRL Global Monitoring Laboratory.” https://gml.noaa.gov/ (accessed Jul. 05, 2021).

[28] “Leistungszahl (COP) – Wärmepumpen Wiki.” https://www.effiziente-waermepumpe.ch/wiki/Leistungszahl_(COP) (accessed Jul. 16, 2021).

[29] J. Peng, L. Lu, and H. Yang, “Review on life cycle assessment of energy payback and greenhouse gas emission of solar photovoltaic systems,” *Renew. Sustain. Energy Rev.*, vol. 19, pp. 255–274, 2013, doi: 10.1016/j.rser.2012.11.035.

[30] R. Frischknecht *et al.*, *Life Cycle Inventories and Life Cycle Assessments of Photovoltaic Systems 2020*, no. June. 2020.

[31] V. M. Fthenakis and H. C. Kim, “Photovoltaics: Life-cycle analyses,” *Sol. Energy*, vol. 85, no. 8, pp. 1609–1628, 2011, doi: 10.1016/j.solener.2009.10.002.

[32] F. Cucchiella and I. Dadamo, “Estimation of the energetic and environmental impacts of a roof-mounted building-integrated photovoltaic systems,” *Renew. Sustain. Energy Rev.*, vol. 16, no. 7, pp. 5245–5259, 2012, doi: 10.1016/j.rser.2012.04.034.

[33] L. Krebs and R. Frischknecht, “Umweltbilanz Strommixe Schweiz 2018, im Auftrag des Bundesamtes für Umwelt (BAFU), 27. April 2021,” no. April, pp. 1–53, 2021, [Online]. Available: https://www.bafu.admin.ch/bafu/en/home/topics/climate/questions-answers.html#2097182071

[34] M. Smith, A. Bevacqua, S. Tembe, and P. Lal, “Life cycle analysis (LCA) of residential ground source heat pump systems: A comparative analysis of energy efficiency in New Jersey,” *Sustain. Energy Technol. Assessments*, vol. 47, no. May, p. 101364, 2021, doi: 10.1016/j.seta.2021.101364.

[35] E. P. Johnson, “Air-source heat pump carbon footprints: HFC impacts and comparison to other heat sources,” *Energy Policy*, vol. 39, no. 3, pp. 1369–1381, 2011, doi: 10.1016/j.enpol.2010.12.009.

[36] B. Greening and A. Azapagic, “Domestic heat pumps: Life cycle environmental impacts and potential implications for the UK,” *Energy*, vol. 39, no. 1, pp. 205–217, 2012, doi: 10.1016/j.energy.2012.01.028.

[37] G. Li, “Comprehensive investigations of life cycle climate performance of packaged air source heat pumps for residential application,” *Renew. Sustain. Energy Rev.*, vol. 43, pp. 702–710, 2015, doi: 10.1016/j.rser.2014.11.078.

[38] Carbotech and Comissioned by SFOE, “Life cycle inventories of heating systems – Switzerland,” no. February, 2021, [Online]. Available: https://www.bafu.admin.ch/dam/bafu/en/dokumente/wirtschaft-konsum/externe-studien-berichte/life-cycle-inventories-of-heating.pdf.download.pdf/life-cycle-inventories-of-heating.pdf

[39] S. Bonn, “Aktualisierte Umwelterklärung 2019,” 2019.

[40] R. Frischknecht *et al.*, “Final report ecoinvent data v2.0, No. 1,” no. 1, 2007, [Online]. Available: https://ecoinvent.org/the-ecoinvent-database/data-releases/ecoinvent-3-0/

[41] sirch, “Sirch vacutherm.” 2013.

[42] S. T.-T. S. GmbH, “Speicher Anfragen-Konfigurator.” https://pufferspeicher-sirch.de/speicher/anfragen-konfigurator/

[43] Energy4me, “energy4me speicherlösungen.”

[44] G. R. Plastic, “ENVIRONMENTAL PRODUCT Glassfiber Reinforced Plastic ( GRP ) Pipes,” 2021.

[45] I. S. Abbood, S. A. Odaa, K. F. Hasan, and M. A. Jasim, “Properties evaluation of fiber reinforced polymers and their constituent materials used in structures - A review,” *Mater. Today Proc.*, vol. 43, pp. 1003–1008, 2021, doi: 10.1016/j.matpr.2020.07.636.

[46] I. Epd, “Environmental Product Declaration - Polyurethane thermal insulation spray foam,” no. Cem Iii, pp. 1–14, 2017, [Online]. Available: http://www.brick.org.uk/wp-content/uploads/2014/01/Please-click-here-to-download-the-EDP.pdf

[47] R. Frischknecht, “UMWELTPRODUKTDEKLARATION NACH NORM SN EN 15804+A1:2013: swissporXPS, Wärmedämmplatten aus extrudiertem Polystyrol,” no. November 2017, pp. 1–7, 2017.

[48] D. Vuarnoz and T. Jusselme, “Temporal variations in the primary energy use and greenhouse gas emissions of electricity provided by the Swiss grid,” *Energy*, vol. 161, pp. 573–582, 2018, doi: 10.1016/j.energy.2018.07.087.

[49] D. Vuarnoz and S. Aguacil Moreno, “Dataset concerning the hourly conversion factors for the cumulative energy demand and its non-renewable part, and hourly GHG emission factors of the Swiss mix during a one-year period (2016 and 2017),” *Data Br.*, vol. 30, p. 105509, 2020,

doi: 10.1016/j.dib.2020.105509.

[50] T. Yang, W. Liu, G. J. Kramer, and Q. Sun, “Seasonal thermal energy storage: A techno-economic literature review,” *Renew. Sustain. Energy Rev.*, vol. 139, no. January, p. 110732, 2021, doi: 10.1016/j.rser.2021.110732.

[51] Y. Sauter and F. Jacqmin, “Photovoltaikmarkt- Beobachtungsstudie 2019,” 2020.

[52] E. Bundesamt, E. B. F. E. Pulverstrasse, I. Postadresse, and B. Infoline, “Photovoltaikmarkt : Preisbeobachtungsstudie 2022,” 2023.

[53] IEA, “Renewable Energy Market Update: Outlook for 2023 and 2024 - International Energy Agency,” p. 87, 2023, [Online]. Available: www.iea.org/t&c/

[54] V. Tulus, D. Boer, L. F. Cabeza, L. Jiménez, and G. Guillén-Gosálbez, “Enhanced thermal energy supply via central solar heating plants with seasonal storage: A multi-objective optimization approach,” *Appl. Energy*, vol. 181, pp. 549–561, 2016, doi: 10.1016/j.apenergy.2016.08.037.

[55] O. Grodzevich and O. Romanko, “Normalization and Other Topics in Multi-Objective Optimization,” *Proc. fields-MITACS Ind. Probl. Work.*, vol. 2, no. August 2006, pp. 89–101, 2006, [Online]. Available: https://www.academia.edu/11635242.

[56] B. Y. J. M. I. Haisman, M. Bush, and S. Wolfe, “TECHNISCHES DATENBLATT STANDARD PLUS X / X+,” *Hand, The*, vol. 5, no. 3, pp. 175–181, 2005.

[57] Dionis Anderegg, Sven Strebel, and Jürg Rohrer, “Photovoltaik Potenzial auf Dachflächen in der Schweiz,” *Zhaw*, 2022.

[58] Bundesamt für Statistik (BFS), “Bau- und Wohnungswesen 2014,” 2016.

[59] M. J. S. Zuberi, K. Narula, S. Klinke, J. Chambers, K. N. Streicher, and M. K. Patel, “Potential and costs of decentralized heat pumps and thermal networks in Swiss residential areas,” *Int. J. Energy Res.*, vol. 45, no. 10, pp. 15245–15264, 2021, doi: 10.1002/er.6801.

[60] FOEN, “Switzerland’s Greenhouse Gas Inventory 1990-2015, National Inventory Report 2017,” *Swiss Fed. Off. Environ.*, no. April, 2017.

[61] “PV*SOL – Valentin Software.” https://valentin-software.com/produkte/pvsol/ (accessed Dec. 13, 2021).